Advanced Materials for Thin-Film Solid Oxide Fuel Cells
Recent Progress and Challenges in Boosting the Device Performance at Low Temperatures

Zhang, Jun; Ricote, Sandrine; Hendriksen, Peter Vang; Chen, Yunzhong

Published in:
Advanced Functional Materials

Link to article, DOI:
10.1002/adfm.202111205

Publication date:
2022

Document Version
Publisher's PDF, also known as Version of record

ADVANCED FUNCTIONAL MATERIALS
www.afm-journal.de

Advanced Materials for Thin-Film Solid Oxide Fuel Cells: Recent Progress and Challenges in Boosting the Device Performance at Low Temperatures

Jun Zhang, Sandrine Ricote, Peter Vang Hendriksen, and Yunzhong Chen*

Solid oxide fuel cells (SOFCs) are efficient and fuel flexible electrochemical energy conversion devices that can power the future green society with regards to homes, cars, and even down to portable electronics. They do have the potential to become low cost, since no noble metals are used. Their broad commercialization, however, is hampered by the high operating temperatures of 700–900 °C. Lowering the operating temperature of SOFCs is challenging as both the charge transport in the solid electrolyte and oxygen exchange reactions are thermally activated processes. Herein, the recent progress in the development of anode, electrolyte, and cathode materials to lower the operating temperature of SOFC below 600 °C is summarized and the new opportunities, as well as challenges that remain to be solved, are discussed. The focus of this review is addressed to thin film SOFCs, sub-micrometer SOFCs (μSOFCs) based on microelectromechanical systems, as well as devices based on proton-conducting oxide electrolyte (protonic ceramic fuel cells), which are especially promising for powering portable devices.

1. Introduction

The generation of electricity in a cost-effective and environmental-friendly way is one of the major challenges for the green transition of our society. Solid oxide fuel cells (SOFCs) can directly convert the chemical energy of hydrogen or hydrocarbons (i.e., propane, butane, methane, or syngas derived from a liquid hydrocarbon) into electricity through electrochemical reactions, and therefore, could have a significant impact on reducing fuel consumption and pollutant emissions.[1–5] The operating principle of fuel cells relies on combining a gaseous fuel (hydrogen, CO, or some hydrocarbons) and an oxidant gas (oxygen from the air) through porous electrodes and an ion-conducting dense electrolyte (**Figure 1**). CO and H_2 are readily converted. Hydrocarbons (gaseous or liquid) need to be decomposed to a synthesis gas first, which may take place outside the SOFC or, in the case of methane to some degree, inside the stack. Depending on the ionic species transported through the electrolyte, SOFCs can be divided into oxygen-ion conductor ceramic fuel cells or proton-conductor ceramic fuel cells. They will be referred to as SOFCs (oxygen ion conductor) and protonic ceramic fuel cells (PCFCs, proton conductor) through this review to comply with the widely used terms in the community. The first-generation SOFC, targeting stationary high-power (in megawatt) applications, was based on a thick yttria-stabilized zirconia (YSZ) electrolyte (>100 μm), which also served as the mechanical support. It requires a high operation temperature above 850 °C to achieve decent power densities. This high-temperature SOFC (HT-SOFC) can be integrated with a gas turbine to maximize the overall efficiency of the power system.[6] For those stand-alone applications, however, a reduction of the operating temperature is beneficial for increasing the durability and lowering the cost of the system. This temperature decrease will lead to slower degradation and enable cheaper materials for balance-of-plant components and metal interconnects. These benefits motivated the development of the second-generation SOFC with the anode providing the mechanical support, permitting the fabrication of thinner YSZ electrolytes (≈10 μm) and, in turn, allowing an operating temperature in the intermediate temperature range (≈700 °C) (IT-SOFC). For example, researchers from Forschungszentrum Jülich demonstrated a high-performance IT-SOFC using thin YSZ electrolyte with both acceptable single cell performance (>1 W cm^{-2}, 0.7 V, H_2 + 3% H_2O as fuel, O_2 as oxidant)[7] and good stability at 700 °C (a stack of two-layer continuously operated for more than 100 000 h at 0.5 A cm^{-2}).[8] The distinct SOFC features of fuel flexibility and high energy density as well as the potential to provide continuous power, are also attractive for the use of SOFC as battery replacement or chargers in the growing market for mobile or portable devices. But such devices often demand rapid start-up and are under higher cost pressure

J. Zhang, P. V. Hendriksen, Y. Chen
Department of Energy Conversion and Storage
Technical University of Denmark
Lyngby 2800 Kgs, Denmark
E-mail: junzh@dtu.dk

S. Ricote
Mechanical Engineering Department
Colorado School of Mines
Golden 80401, USA

Y. Chen
Beijing National Laboratory for Condensed Matter Physics
and Institute of Physics
Chinese Academy of Sciences
Beijing 100190, China

The ORCID identification number(s) for the author(s) of this article can be found under https://doi.org/10.1002/adfm.202111205.

DOI: 10.1002/adfm.202111205

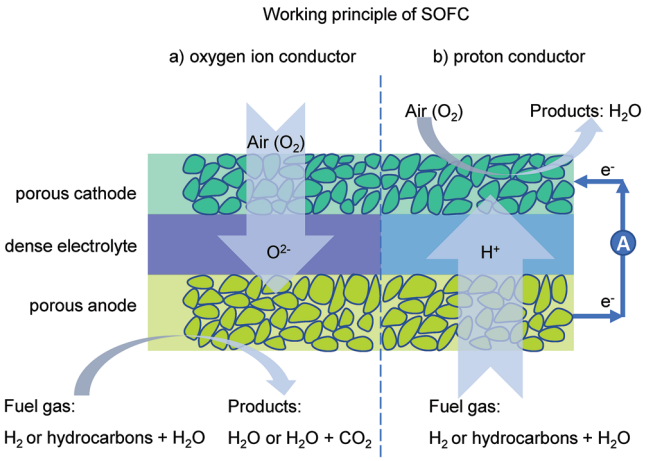

Figure 1. Working principle of SOFC with i) an oxygen-ion conductor electrolyte (SOFC) and ii) a proton-conducting electrolyte (PCFC).

pushing for a further decrease of the operating temperature from 700 °C toward 600 °C or even 500 °C (low-temperature SOFC, LT-SOFC).[9–13] The main challenge in this endeavor is maintaining sufficiently high performance (above 1 W cm^{-2}) at such low temperatures since the resistance from the electrolyte and both electrodes increase significantly due to the thermally activated nature of the underlying transport and electrode processes. It is, thus, important to design novel materials and structures for the electrolyte and electrodes to enable higher conductivity and electrochemical kinetics at low temperatures.

Despite the challenges, considerable advances have been achieved in recent years regarding materials and novel structure developments (**Figure 2**a). The resulting boost in the device performance below 600 °C (Figure 2b) shows the potential for using SOFC technology in distributed and even mobile applications. These include the advances in the fabrication of nanostructured electrodes, the replacement of the O^{2-} conducting electrolyte with H^+ conducting one, as well as the ability to internally reform hydrocarbon fuels at the anode. Notably, an exceptional power density at low temperature, 0.5 W cm^{-2} at 500 °C, has been achieved in a PCFC.[14]

Herein, we summarize the recent progress and discuss the strategies in terms of thin film and advanced material development to develop the next-generation LT-SOFCs, with a focus on device performance. In addition to the traditional LT-SOFC with an oxygen ion-conducting electrolyte, LT-SOFCs with a proton-conducting electrolyte (PCFC) and sub-micrometer solid oxide fuel cell (μSOFC) with extremely thin electrolyte (in sub-micrometer scale) are both included in this review. For each category, we first introduce the core challenges that emerged for the electrolyte, anode, and cathode at low temperatures. The recent approaches to addressing those difficulties are then highlighted, followed by a discussion of the unsolved tasks which need further investigation.

2. Advanced Materials for LT-SOFCs

The LT-SOFC targets operation in the 300–600 °C temperature range and can, in principle, be divided into two major groups: 1) the micrometer scale SOFC by combining both thin-film and conventional ceramic technologies and 2) the μSOFC based on microelectromechanical systems (MEMS).

2.1. LT-SOFC with Key Components within Micrometer Scale

In recent years, researchers have focused on lowering the operating temperature of conventional ceramic-based SOFCs. Since the thick electrolyte supported geometries lead to high ohmic resistance in the low operation temperature regime, anode support configurations tend to be the route taken for LT-SOFCs. Moreover, to cope with the challenges related to lowering the operation temperature (e.g., decreased electrolyte conductivity and sluggish electrocatalytic activity of the electrodes), progress has been made to identify new electrolyte materials with higher conductivity, fabricate thin-film electrolyte layer with high quality, and develop more active electrodes.[7,16] The term "area-specific resistance, ASR (the resistance normalized to the active fuel cell area, in units of Ω cm^2)" is used to describe the electrolyte or electrode activity loss quantitatively. An ASR of less than 0.1 Ω cm^2 for each component (electrolyte, anode, and cathode) is normally targeted in the community.[1,2,11,12] Such an ASR requirement can be achieved down to 475–500 °C with a thin and highly conductive electrolyte and highly active electrodes used in the state-of-the-art LT-SOFCs (**Figure 3**). However, with lower temperatures, the ASR increases significantly, especially for the electrodes.

2.1.1. O^{2-}-LT-SOFC

Electrolytes for O^{2-}-LT-SOFC: Among the potential electrolyte materials, oxygen-ion conductor YSZ has been the electrolyte material for HT-SOFC because of its good ionic conductivity and mechanical and chemical stability under fuel cell operating conditions. A thinner YSZ, however, is required for LT-SOFC to meet the electrolyte requirement of area-specific resistance (ASR_{el}) of 0.1 Ω cm^2, as mentioned above. **Figure 4** compares the temperature-dependent ionic conductivity and the required thickness by the ASR_{el} target for some typical electrolyte materials. For YSZ, the electrolyte thickness to meet the ASR_{el} requirement is 10 μm at 700 °C and 1 μm at 500 °C. Fabricating such a thin gas-tight layer on large area (a few cm^2) ceramic substrates is technically challenging and presently costly. Alternative electrolyte materials with higher ionic conductivity are displayed in Figure 4: gadolinia-doped ceria (GDC), strontium, and magnesium-doped lanthanum gallate (LSGM), and dysprosium- and tungsten-stabilized bismuth oxide (DWSB). The conductivity of GDC is nearly one order of magnitude higher than that of YSZ, suggesting that the ASR_{el} requirement at 500 °C can be met for a 10 μm GDC (instead of a 1 μm YSZ). However, all the electrolyte materials that exhibit a higher ionic conductivity than YSZ are either chemically unstable or present compatibility issues. For example, GDC is known to have serious Ce^{3+} reduction ($Ce^{4+} \rightarrow Ce^{3+}$) under reducing atmospheres at temperatures above 600 °C, causing an internal current short circuit and chemical expansion in the electrolyte layer, harmful to the cell performance and long-term mechanical stability.[43–45] However, since the reduction reaction in ceria

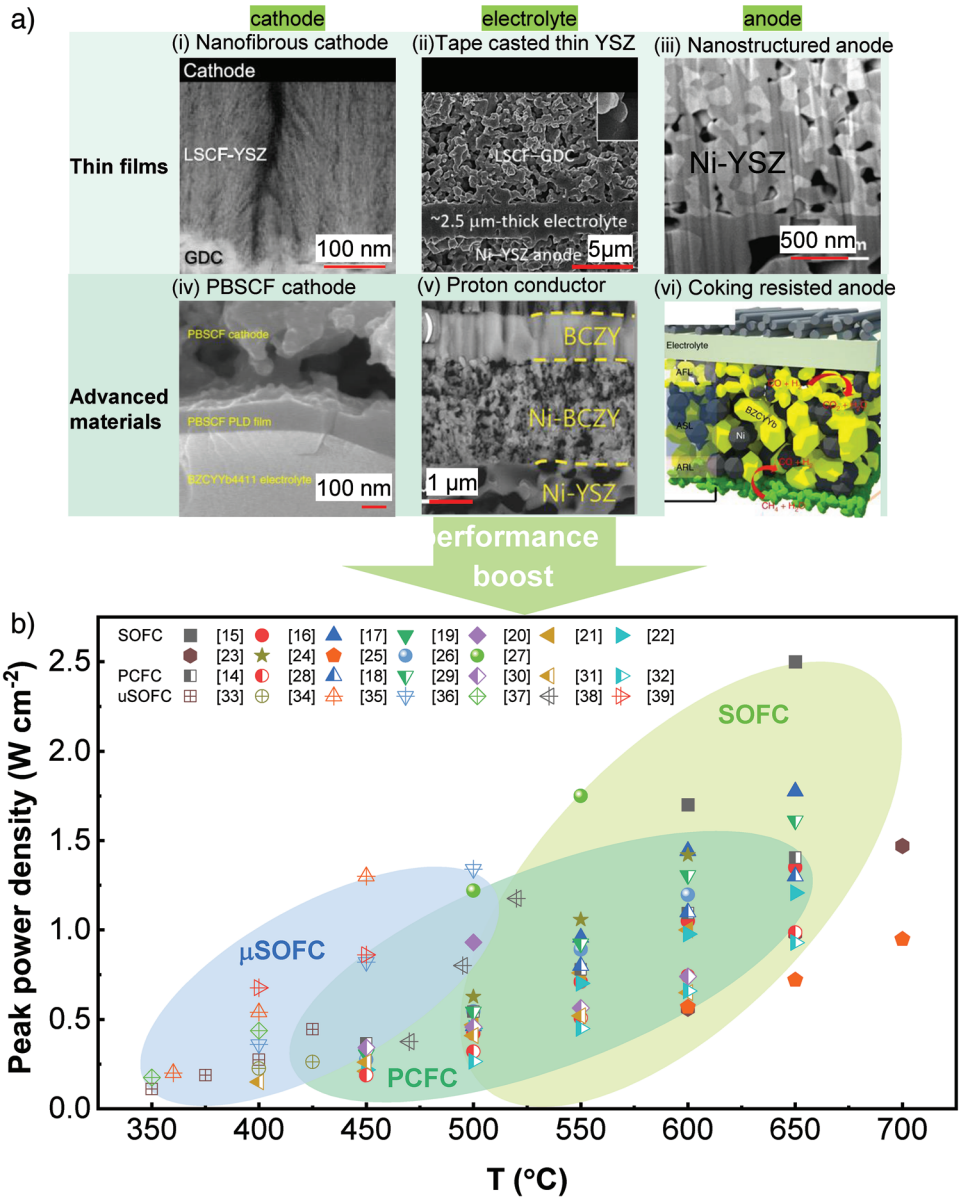

Figure 2. a) Recent advances in the thin film and materials development for SOFC for boosting the single-cell performance. (a-i) Reproduced with permission.[15] Copyright 2020, American Chemical Society, (a-ii) Reproduced with permission.[16] Copyright 2012, Wiley-VCH GmbH & Co. KGaA, Weinheim. (a-iii) Reproduced with permission.[17] Copyright 2016, Elsevier B.V. (a-iv) Reproduced with permission.[14] Copyright 2018, Springer Nature Limited. (a-v) Reproduced with permission.[18] Copyright 2018, Wiley-VCH GmbH & Co. KGaA, Weinheim. (a-vi) Reproduced with permission.[19] Copyright 2018, Springer Nature Limited. b) Peak power density comparison for different SOFC categories at different temperatures (SOFC:[15–17],[19–27] PCFC:[14,28,18,29–32] µSOFC:[33–39]). LSCF: $La_{0.6}Sr_{0.4}Co_{0.2}Fe_{0.8}O_{3-\delta}$, PBSCF: $PrBa_{0.5}Sr_{0.5}Co_{1.5}Fe_{0.5}O_{5+\delta}$, BCCY: $BaCo_{0.7}(Ce_{0.8}Y_{0.2})_{0.3}O_{3-\delta}$, BCZY: $BaCe_{0.55}Zr_{0.3}Y_{0.15}O_{3-\delta}$, BZCYYb: $BaZr_{0.1}Ce_{0.7}Y_{0.1}Yb_{0.1}O_{3-\delta}$. Please note that the above broad comparison illustrates reachable power density levels. Some reports are for button cells, while some are for technologically relevant cell sizes >100 cm^2. One should appreciate that the peak power density under technologically relevant conditions may be lower than numbers quoted in (b) due to limitations set by heat management issues and that often, to compete with alternative technologies for a specific segment, SOFC has to be run at higher efficiency but lower power density.

is less temperature-dependent than the H_2/H_2O equilibrium, the problem is alleviated with lowering temperature: below 550 °C the consequences of an electronic short and the chemical expansion become negligible.[40,43,46] The challenge with LSGM lies in finding a compatible fuel electrode material, as it reacts with Ni, the state-of-the-art anode material, to form a highly resistive phase.[47] DWSB undergoes a phase transformation to a low ionic conductive phase under reducing atmospheres.[48] Therefore, current electrolyte development for O^{2-} conducting LT-SOFC follows two strategies: 1) fabricating an extremely thin and dense YSZ electrolyte layer with a target of ≤1 µm in a reliable and cost-effective way and 2) stabilizing the other potential oxide ion-conductors that have a conductivity higher than YSZ (GDC, LSGM, DWSB...).

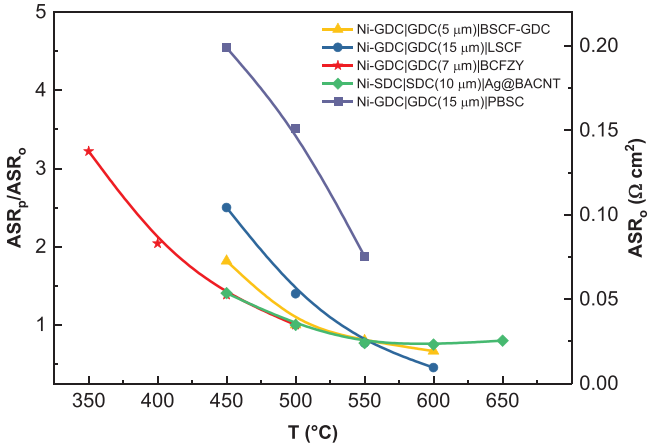

Figure 3. The left *y*-axis represents the ASR ratio of total electrode (ASRp, anode, and cathode) to electrolyte (ASR$_o$) measured from asymmetric cells under open-circuit voltage conditions using air as oxygen and humidified H_2 (3–10% H_2O) as fuel. While the right *y*-axis represents the specific ASR$_o$ value. The notation XX|XX|XX means the anode |electrolyte(thickness)|cathode material. Ni-GDC|GDC|BSCF-GDC,[40] Ni-GDC|GDC|LSCF,[26] Ni-GDC|GDC|BCFZY,[41] Ni-SDC|SDC|Ag@BACNT,[21] Ni-GDC|GDC|PBSC.[42] GDC: gadolinia-doped ceria, SDC: scandia-doped ceria, LSCF: $La_{0.6}Sr_{0.4}Co_{0.2}Fe_{0.8}O_{3-\delta}$, BSCF: $Ba_{0.5}Sr_{0.5}Co_{0.8}Fe_{0.2}O_{3-\delta}$, BCFZY: $BaCo_{0.4}Fe_{0.4}Zr_{0.1}Y_{0.1}O_{3-\delta}$, BACNT: $Ba_{0.95}Ag_{0.05}Co_{0.8}Nb_{0.1}Ta_{0.1}O_{3-\delta}$, PBSC: $PrBa_{0.5}Sr_{0.5}Co_2O_{5+\delta}$.

Regarding the fabrication of thin YSZ electrolytes, we want to highlight two remarkable studies on the successful development of a dense 1 µm YSZ electrolyte using highly scalable fabrication techniques. The first one is by Han et al., who reported a procedure to fabricate a 1 µm gas-tight YSZ electrolyte layer onto an "industrial-scale" (5 × 5 cm^2) anode substrate (NiO/YSZ). Through a series of steps (spin coating and calcination of YSZ

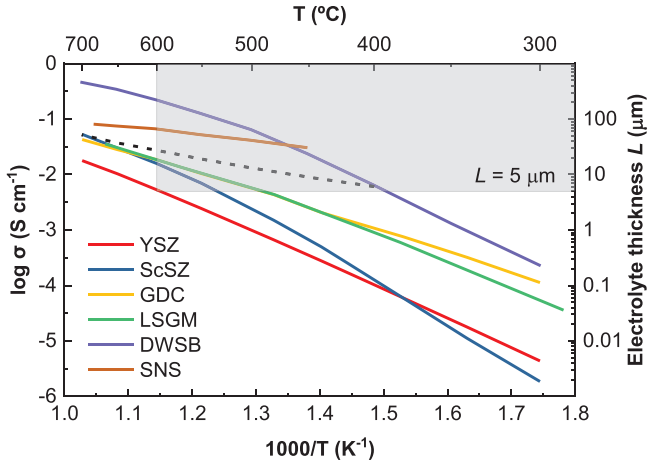

Figure 4. Comparison of ionic conductivity (measured under air atmosphere) of various solid oxide electrolytes with the shadow area indicating below 600 °C the available electrolyte materials to meet the ASR$_{el}$ target of 0.1 Ω cm^2 for a thickness above 5 µm. YSZ: yttria-doped zirconia,[49] ScSZ: scandia-doped zirconia,[49] GDC: gadolinia-doped ceria,[49] LSGM: strontium and magnesium doped lanthanum gallate,[50] DWSB: dysprosium- and tungsten-stabilized bismuth oxide,[51] SNS: $Sr_{3-3x}Na_{3x}Si_3O_{9-1.5x}$.[52] The dashed line is indicative of the conductivity of a BZCYYb ($BaZr_{0.1}Ce_{0.7}Y_{0.2-x}Yb_xO_{3-\delta}$) proton conductor,[53] which will be discussed in detail in the following section of PCFC electrolyte.

nanosuspension and polymetric gel with optimized viscosity), they obtained a dense 1 µm YSZ electrolyte after sintering at 1400 °C for 5 h. The high-quality thin YSZ results in an ASR$_{el}$ as low as 0.17 Ω cm^2 at 550 °C.[7] The second one is from Nédélec et al., who sputtered (DC power) a 1 µm gas-tight YSZ electrolyte layer on a substrate without pretreatment. Increasing the bias power during the sputtering changed the sputtered microstructure from columnar to dense defect-free.[54] These two studies illustrate a potentially low-cost, scalable, and reliable way to fabricate thin YSZ electrolytes for the LT-SOFC.

In addition to YSZ, the so-called "bilayer electrolyte" strategy has been widely investigated for LT-SOFC:[16,20,43,45,55–57] it consists of adding a YSZ layer on the GDC electrolyte to block the electronic conduction. For example, Myung et al. compared an LT-SOFC with a single GDC electrolyte layer and a similar cell after the insertion of an ultrathin (200 nm) YSZ blocking layer.[45] The open-circuit voltage (OCV) and the peak power density at 600 °C increased from 0.6 to above 1 V and from 0.377 to 1 W cm^{-2}, respectively. However, the challenges for this bilayer electrolyte (YSZ/GDC) lie in their poor material compatibility at high temperatures and higher resistance of YSZ: the interdiffusion of the Zr- and Ce-phases during the high-temperature electrolyte sintering (≈1200 °C)[58–61] hampers the conductivity. In addition, the YSZ layer needs to be extremely thin to minimize its resistance contribution. Two main approaches have been applied to address these issues. The first one is to fabricate dense YSZ/GDC bilayer electrolyte below 900 °C to limit cation interdiffusion, for example, through the physical vapor deposition techniques.[45,56,57] The second approach employs lowering the densification temperature of the YSZ using sol–gel of nanoparticles[16] or adding suitable sintering aids.[23] Recently, Park and Barnett were able to fabricate a 2.5 µm bilayer electrolyte made of 1.5 µm YSZ and 1 µm GDC (**Figure 5**b) using tape casting and dip coating (details on the size of the substrate support are not provided). Reducing the electrolyte thickness from 8 µm (t8 cell, Figure 5a) to 2.5 µm (t2.5 cell) resulted in an ohmic resistance decrease (Figure 5c) and a 70% performance enhancement at 600 °C (Figure 5d).[23] It is important to note that it might still be possible to use single GDC cells at temperatures below 550 °C because of the minimized GDC reduction at lower temperatures.[43,62,63] Lee et al. recently demonstrated a high-performance SOFC with a single 5 µm thick GDC electrolyte, 1.58 W cm^{-2} at 500 °C. The single GDC yields an OCV of 0.96 V, indicating minor internal current leakage in the electrolyte.[40] Moreover, when targeting stack operation at "modest" efficiency and high-power density (e.g., operating at a voltage between 0.5 OCV and 0.75 OCV at low temperatures $T < 550$ °C), the issues related to electronic leakage in CGO are manageable, as discussed by Dalslet et al.[46]

Cathodes for O^{2-}-LT-SOFC: This section focuses on strategies to improve the low-temperature performance of SOFC cathodes. For more comprehensive reviews on oxygen electrodes, the following references are recommended.[10,11,64–67]

An SOFC cathode material must catalyze the bond-breaking of the oxygen molecule, be able to accept electrons from the external circuit, and enable facile delivery of oxygen ions to the electrolyte. The overall oxygen reduction reaction (ORR) reads as $1/2O_2(g) + 2e^-(\text{cathode}) \rightarrow O^{2-}(\text{electrolyte})$. This process may take place via a series of elementary reactions: adsorption of oxygen on the cathode surface; dissociation and ionization

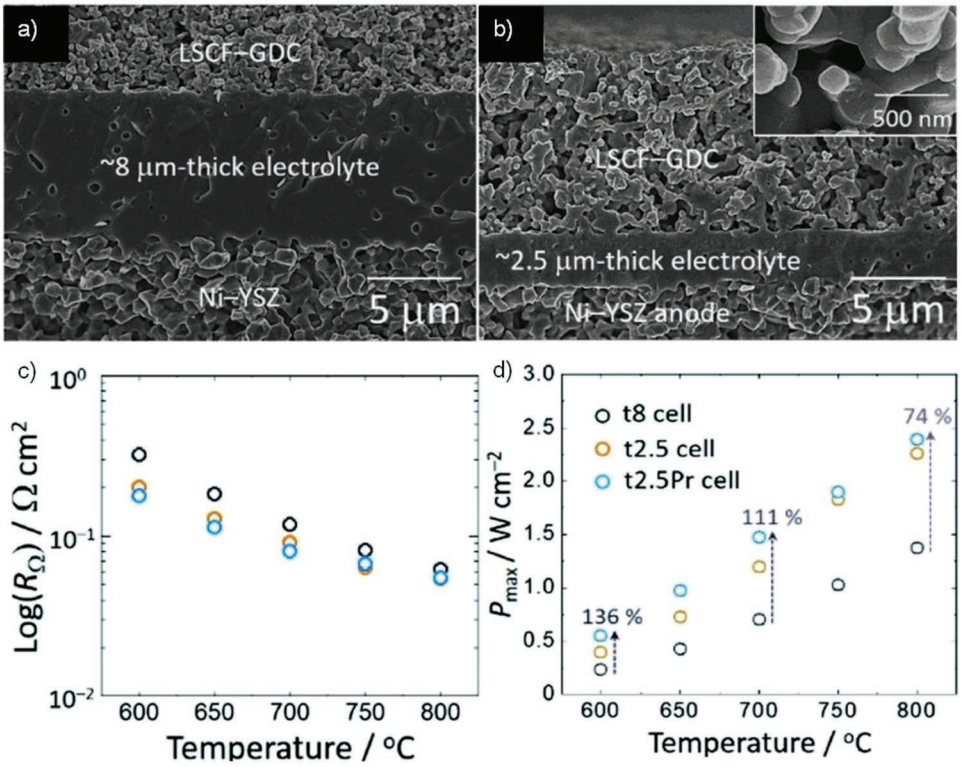

Figure 5. Fracture cross-sectional SEM images of a) the baseline cell with 8 µm electrolyte (t8 cell) and b) the cell with reduced (2.5 µm) thickness (t2.5 cell). Comparison of c) ohmic (R_Ω) resistance and d) maximum power densities (P_{max}) as a function of temperature. Reproduced with permission.[23] Copyright 2020, The Royal Society of Chemistry.

of oxygen to oxide ions; incorporation of oxide ions into oxygen vacancies; and finally transportation to the electrolyte.[68,69] Because of the high activation energy (i.e., ≈1.3–1.8 eV) for the ORR, the cathode becomes critical for cell performance with decreasing temperature.[10,11,70] Therefore, significant focus has been placed on searching for more electrochemically active cathode materials[27,41,71] or enhancing the ORR of conventional cathodes at low temperatures via morphology optimization[15,40,72] or functionalization via infiltration.[23,73,74] There are three perovskite-related material classes for which high performance at low temperatures has been reported: $ABO_{3-\delta}$ perovskites, $AA'B_2O_{5+\delta}$ double layer perovskites, and $A_2BO_{4+\delta}$ Ruddlesden–Popper (RP) phases. Their structures are shown in **Figure 6** a, while the cathode area-specific resistances (ASR_c) are compared in the 450–700 °C temperature range in Figure 6b for a wide range of material belonging to these classes.

$ABO_{3-\delta}$ Perovskites: The Sr-doped $LaMnO_3$ perovskite, $La_{1-x}Sr_xMnO_{3-\delta}$ (LSM), is a classical cathode material for conventional high-temperature SOFCs (>800 °C), owing to its good electronic conductivity, thermal and chemical stability under SOFC operating conditions.[85] However, its poor ionic conductivity causes large polarization resistance at reduced temperature (55.7 Ω cm^2 at 700 °C compared with 0.39 Ω cm^2 at 900 °C[86]) and limits its application to high temperatures. Therefore, for the LT-SOFC, the focus has been shifted to mixed ionic and electronic conductors (MIECs), such as $La_{1-x}Sr_xCoO_{3-\delta}$ (LSC). LSC exhibits an ASR_c of 0.023 Ω cm^2 at 600 °C when used as a nanoporous LSC cathode film layer.[72] Two factors could explain this high performance: first, the electronic structure of undoped $LaCoO_3$ is in a rather high electron density occupation of crystal field d states near the Fermi level, facilitating the electron transfer between a surface cation and an interacting oxygen molecule;[87] second, the two coexisting charge compensating mechanisms (formation of Co^{4+} and oxygen vacancies from Sr doping) improve the MIEC properties.[88] Moreover, the significant oxygen vacancy concentration and mobility under air also facilitate the ORR.[89] Whereas Co-containing cathode materials excel due to their high electrochemical activity, the practical application is challenged by the chemical expansion related to loss of oxygen with increasing temperature: Their very high apparent thermal expansion coefficient (TEC) (≈20×10^{-6} K^{-1}) in the desired operating temperature range can cause delamination at the interface between the LSC cathode and some common electrolytes (YSZ, GDC, ScSZ, LSGM, whose TECs are in the range of 10–12×10^{-6} K^{-1}[64]). Partial substitution of Co by Fe, $La_{1-x}Sr_xCo_yFe_{1-y}O_{3-\delta}$ (LSCF) significantly decreases the TEC mismatch while maintaining electrochemical performance close to that of LSC. For example, the TEC can be reduced to 15×10^{-6} K^{-1}[90] for $y = 0.2$ while keeping a low ASR_c of 0.13 Ω cm^2 at 600 °C.[75] The thermomechanical challenges can also be alleviated with composite electrodes.[91] Conventional composites are prepared by mixing the electrocatalyst with the electrolyte material (particle size in the range of ≈1 µm). A finer microstructure can be achieved with a nanoparticulate coverage of a "backbone structure" electrolyte with the electrocatalyst (infiltration or exsolution). For example, by

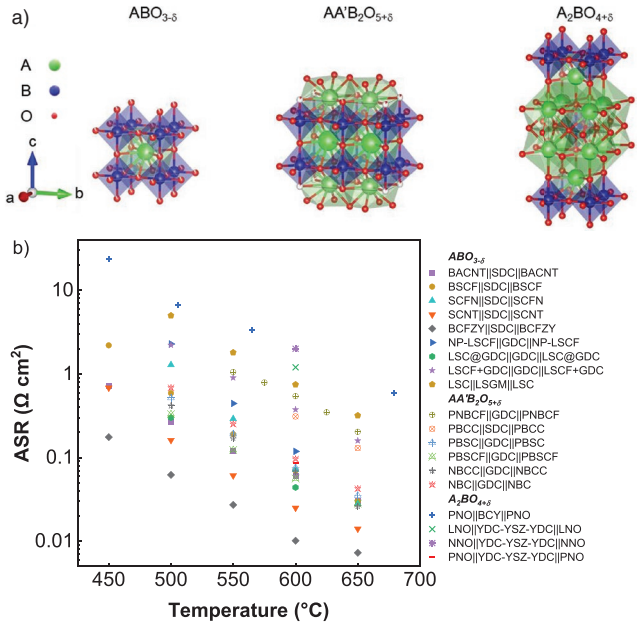

Figure 6. a) Illustration of the structures of an ABO_3 perovskite, a double layer perovskites $AA'B_2O_{5+\delta}$, and the end member of a Ruddlesden–Popper-type compound $A_2BO_{4+\delta}$. b) Cathode ASRc comparison of some representative cathodes for each category, measured in asymmetrical cell configuration (electrode‖electrolyte‖electrode) in air. $ABO_{3-\delta}$:BACNT ($Ba_{0.95}Ag_{0.05}Co_{0.8}Nb_{0.1}Ta_{0.1}O_{3-\delta}$),[21] BSCF ($Ba_{0.5}Sr_{0.5}Co_{0.8}Fe_{0.2}O_{3-\delta}$),[71] SCFN ($Sr_{0.9}Ce_{0.1}Fe_{0.8}Ni_{0.2}O_{3-\delta}$),[22] SCNT ($SrCo_{0.8}Nb_{0.1}Ta_{0.1}O_{3-\delta}$),[27] BCFZY ($Ba(Co_{0.4}Fe_{0.4}Zr_{0.1}Y_{0.1})_{0.95}O_{3-\delta}$),[24] NP-LSCF (nano ($La_{0.6}Sr_{0.4}Co_{0.2}Fe_{0.8}O_{3-\delta}$),[75] LSC ($La_{0.6}Sr_{0.4}CoO_{3-\delta}$)@GDC,[74] LSCF+GDC,[76] LSC;[77] $AA'B_2O_{5+\delta}$: PNBCF ($Pr_{0.8}Nd_{0.2}BaCo_{1.6}Fe_{0.4}O_{5+\delta}$),[78] PBCC ($PrBa_{0.8}Ca_{0.2}Co_2O_{5+\delta}$),[25] PBSC ($PrBa_{0.5}Sr_{0.5}Co_2O_{5+\delta}$), and PBSCF ($PrBa_{0.5}Sr_{0.5}Co_{1.5}Fe_{0.5}O_{5+\delta}$),[79] NBCC ($NdBa_{0.75}Ca_{0.25}Co_2O_{5+\delta}$) and NBC ($NdBaCo_2O_{5+\delta}$);[80] $A_2BO_{4+\delta}$:PNO ($Pr_2NiO_{4+\delta}$),[81] LNO ($La_2NiO_{4+\delta}$),[82] NNO ($Nd_2NiO_{4+\delta}$),[83] PNO.[84]

infiltrating Pr_6O_{11} nanoparticles into LSCF/CGO composite electrodes, Khoshkalam et al. decreased the ASR_c by a factor of 4 to 0.081 Ω cm² at 600 °C.[92] The superiority may in part come from Pr dissolving in the ceria ($Pr_xCe_{1-x}O_{2-\delta}$ (PCO)), which leads to a much higher electronic conductivity than in GDC because of electron hopping between mixed-valence Pr sites (Pr^{4+} is easily reduced to Pr^{3+} even under oxidizing atmosphere).[93,94] PrO_x-based infiltrated electrodes were observed to be fairly stable over a 220 h impedance test.[92] It is important to note that the risk of delamination scales with the layer thickness and the square of the TEC mismatch.[95] Hence large TEC mismatches can be tolerated for thin layers.

Another material, $Ba_{1-x}Sr_xCo_yFe_{1-y}O_{3-\delta}$ (BSCF), initially designed to increase the phase stability of the oxygen separation membrane material, $SrCo_yFe_{1-y}O_{3-\delta}$ (SCF),[96] has been studied in some detail since its first SOFC application reported by Shao et al. in 2004. They reported a remarkably low ASR_c: 0.055–0.071 Ω cm² at 600 °C. In addition to the superior oxygen ion bulk diffusion, Suntivich et al. found that the excellent catalytic effects of BSCF could come from its Co electronic structure, with e_g configuration close to unity ($t_{2g}^5e_g^{\approx 1.2}$) facilitating the binding of oxygen intermediates to the oxide surface.[97] However, the oxygen surface exchange reaction of BSCF slows significantly below 500 °C, causing an ASR_c around 0.5 Ω cm², nearly one order of magnitude higher than at 600 °C.[71] Moreover, the material shows a phase transformation at low temperature which may challenge thermomechanical integrity.[98,99]

Recently, Li et al. discovered a novel cathode material with promising performance below 500 °C: $SrCo_{0.8}Nb_{0.1}Ta_{0.1}O_{3-\delta}$ (SCNT), which exhibits extremely low ASR_c of 0.16 and 0.68 Ω cm² at 500 and 450 °C, respectively. Through a systematic investigation of SCNT, SCT ($SrCo_{0.8}Ta_{0.2}O_{3-\delta}$), and SCN ($SrCo_{0.8}Nb_{0.2}O_{3-\delta}$), they found that the superior electroactivity of SNCT comes from the codoping of Nb and Ta in the B-site. The Ta-doping increases the oxygen vacancy concentration (the oxygen vacancy concentrations of SCNT, SCT, and SCN are 0.168, 0.159, and 0.102, respectively) while the Nb doping induces a higher density of electronic states of the Co atoms near the Fermi level (98% for the SCNT compared with 60% for the SCT),[27] which could facilitate the electron transfer in the oxygen reduction reaction.[100]

$AA'B_2O_{5+\delta}$ Double Layer Perovskites: With 50% substitution of the A-site in ABO_3 perovskite with lower-valence A′ cations, a new double-layer perovskite with the general formula $AA'B_2O_{5+\delta}$ (A, rare earth element; A′, alkaline earth; B, Co, or Mn) can be obtained. The $AA'B_2O_{5+\delta}$ compounds have an ordered layer structure of −[A′O][BO_2][$AO_{1-\delta}$][BO_2]− in the *c*-direction (Figure 6a)), similar to the structure of the cuprate superconductors.[79] The enhanced and anisotropic oxygen diffusion in the [AO] plane,[101–103] together with high oxygen exchange coefficients[104] and high electronic conductivity,[105] make $AA'B_2O_{5+\delta}$ attractive cathode materials for LT-SOFC.

Most of the studied $AA'B_2O_{5+\delta}$ as SOFC cathodes have focused on the $LnBaCo_2O_{5+\delta}$ (for example, Ln = La, Pr, Nd, Sm, and Gd) system. It is found that the thermal expansion coefficient, the oxygen content 5+δ, the electrical conductivity, and the catalytic activity for the oxygen reduction reaction are closely related to the ionic radius of the Ln^{3+}. A general trend is that the electrical conductivity and the thermal expansion coefficient decrease with the decreasing Ln^{3+} ionic radius size.[106,107] The ASRc of the individual $LnBaCo_2O_{5+\delta}$ for the oxygen reduction reaction is ranked as follows Ln^{3+}: Pr^{3+} < Gd^{3+} < Nd^{3+} < Sm^{3+} < La^{3+}. Taking one specific example, the low ASR_c of $PrBaCo_2O_{5+\delta}$ (PBCO) ranges between 0.15 and 0.21 Ω cm² at 600 °C.[104,107] Under fuel cell operation conditions, a cell of PBCO/$Ce_{0.8}Sm_{0.2}O_{1.9}$/Ni-$Ce_{0.8}Sm_{0.2}O_{1.9}$ achieved a maximum power density of 0.62 W cm^{-2} at 600 °C.[108] The outstanding performance for PBCO is probably related to the dominating role of the electrical conductivity and mixed valence state of Pr^{3+} as well as its counteracting ionic size effects for the larger Ba^{3+} in the same A site. The high TEC of PBCO (~20–25 × 10^{-6} K^{-1}[109,110]) can be partially alleviated by lowering the Co content with, for example, the partial substitution by Ni,[110] Fe,[96] and Cu.[111] The TEC of the Co-free $PrBaFe_2O_{5+\delta}$ composition, ≈17 × 10^{-6} K^{-1},[109] is still somewhat high compared to the common electrolyte materials like YSZ and GDC (with TEC in the range of 10–12 × 10^{-6} K^{-1}).

$PrBa_{0.5}Sr_{0.5}Co_{1.5}Fe_{0.5}O_{5+\delta}$ (PBSCF) is a typical example of the synergistic effect of codoping both the A-site and B-site resulting in a low ASR_c (0.056 Ω cm²) and high peak power densities of >2 W cm^{-2} at 600 °C when tested in Ni-CGO/CGO/PBSCF cell.[79] Further understanding the mechanism for the accelerated oxygen reduction reaction in PBSCF is necessary to

tailor its microstructure and composition and further advance its potential as cathode material in LT-SOFC. Due to the high TEC ($\approx 20 \times 10^{-6}$ K^{-1}),[112] this material is most likely to be best used in a composite where it is mixed with the electrolyte or as a thin skin layer realized via infiltration.

$A_2BO_{4+\delta}$ Ruddlesden–Popper Phases: In addition to the perovskites, the A_2BO_4 oxides, with structure of ···[AO][BO_2][AO][AO][BO_2]··· along the *c*-direction (Figure 6a), have also been investigated as cathode materials for LT-SOFCs. The advantage of such a structure is its ability to accommodate interstitial oxygens in the rock-salt AO layers, leading to high (but directional[113]) oxygen ionic conductivity without the need for A-site substitution. Therefore, the long-term stability for this class of material might be improved as A-site substitutions are prone to surface segregation, which may impede oxygen exchange.[114]

The most widely studied RP phases for SOFC cathodes are the Ln_2NiO_4 (Ln = La, Pr or Nd) oxides with K_2NiF_4-type structure. On the one hand, these oxides exhibit excellent oxygen transport properties (oxygen diffusion and surface exchange coefficients, D^* and k, comparable to that of some well-known perovskites such as BSCF, LSC, and LSCF[115,116]), reasonable electronic conductivity (≈100 S cm^{-1} at 700 °C), and a relatively low TEC ($\approx 13 \times 10^{-6}$ K^{-1}, closely matchable with those of commonly used electrolyte material such as YSZ, GDC, and LSGM), making them "ideal" electrode materials for SOFC.[117–119] On the other hand, the drawbacks include the one-directional nature of the fast ionic transport[113] and their chemical/thermal stability issues with the most common electrolyte materials: 1) La_2NiO_4 (LNO) reacts with YSZ and CGO above 900 and 700 °C, respectively, 2) Nd_2NiO_4 (NdNO) reacts with YSZ and CGO above 1000 °C, and 3) Pr_2NiO_4 (PNO) is not thermally stable above 900 °C even in air.[120] Another drawback is the relatively large ASRc at reduced temperature: ASRc values of 4.1, 2.1, and 0.55 Ω cm^2 were reported at 600 °C for LNO, NdNO, and PNO, respectively.[121] However, recently Ferchaud et al.[84] and Railsback et al.[122] both demonstrated that fast cathode reactions could be obtained on nickelates at low temperatures with microstructure optimization. ASR_c values as low as 0.08 and 0.2 Ω cm^2 were reported for a porous PNO electrode and for a PNO-infiltrated LSGM backbone at 600 °C, respectively. Given such competitive resistance of the modified PNO electrodes and the absence of the chemical instability issues related to the A-site dopant segregation in perovskites, more intensive investigation in solving RP phases' compatibility issues with the electrolyte materials is warranted.

Another attractive application of A_2BO_4 materials is compositing them with a perovskite to establish heterointerfaces between the two phases, which may provide high activity. Sase et al. observed a precipitated secondary phase ($(La_{0.5}Sr_{0.5})_2CoO_4$ (LSC_{214}) during a heat treatment of ($La_{0.6}Sr_{0.4}$)CoO_3 (LSC_{113}), and measured orders of magnitude faster oxygen exchange along their interface at 500 °C.[123] The same phenomenon was also observed by other groups later.[124–126] The mechanism behind this ORR activity enhancement in ABO_3/A_2BO_4 heterostructure is still under investigation. It is hypothesized that the change in electronic structure causes such an enhancement: when the p-type LSC_{214} is in contact with LSC_{113}, LSC_{214} loses its energy gap at the surface, being considerably enriched in free electrons, and facilitates the fast reduction of oxygen at the LSC_{214} surface.[127] Besides, cation segregation could be another explanation with the two following observations: LSC_{214} decoration increases Sr segregation from LSC_{113} to its interface with LSC_{214},[128] and a highly active secondary phase (a metastable Co-deficient perovskite phase $La_{0.7}Sr_{0.3}Co_{0.9}O_{3-\delta}$) formed at the heterointerface.[124] Identifying the detailed mechanism behind this ORR activity enhancement has great potential for optimizing the LT-SOFC cathodes.

Nanoscale Cathode Improvement: Besides the cathode material development, as recently reviewed by Irvine et al.,[129] the critical region governing the SOFC performance is normally at the electrolyte and electrode interface, where the best performance involves intricate structure design on the nanoscale. Lee et al. confirmed this by fabricating a high-performance LSCF/YSZ cathode composite with a nanofibrous microstructure (realized by magnetron sputtering) (**Figure 7**a). The extremely fine nanofibrous structure, with a diameter of several nanometers and relatively large vertical pores between the columns, ensures high mass transport of oxygen to the whole cathode and provides a large active surface area. It resulted in a small ASR_c of around 0.15 Ω cm^2 and a peak power density of 1.7 W cm^{-2} at 600 °C (Figure 7b,c).[15] Through sol–gel coating of a nanoscaled LSC thin film cathode on the GDC electrolyte, Dieterle et al. achieved a record low ASR_c of 0.023 Ω cm^2 at 600 °C.[72] The claimed reasons for the high cathode performance are the high porosity of 45% (attributed to the nanocrystallinity) and the high density of segregated Co_3O_4 (which is believed to be beneficial for the oxygen surface exchange[114]). Therefore, these examples demonstrate that the "traditional well-performing" high-temperature cathode materials can still be used for low-temperature applications with structural and compositional optimization.

Chen et al. could significantly increase the ORR rate of an LSCF cathode with the coating of a thin $PrBaCaCo_2O_{5+\delta}$ (PBCCO) film (illustrated in **Figure 8**a). After cofiring with the LSCF cathode at 800 °C for 1h, some nanoparticles of $BaCoO_{3-x}$ and $PrCoO_{3-x}$ segregated from PBCCO. The nanoscale microstructure (Figure 8b–d) of these multiphase (MP) catalysts ($BaCoO_{3-x}$ and $PrCoO_{3-x}$ nanoparticles and PBCCO film)-coated LSCF cathode (MP-LSCF) confirms the double perovskite structure of the uniformly coated epitaxial catalyst layer with thickness around 30 nm. With the synergetic effects of the nanoparticles and the thin PBCCO film, the ASR_c of the MP-LSCF was effectively reduced to ≈0.312 Ω cm^2 at 600 °C, eightfold lower than that of the bare LSCF cathode (≈2.57 Ω cm^2) under the same conditions (albeit still falling a factor 10 short of what has been achieved on infiltrated Pr_6O_{11} on GDC backbone (0.03 Ω cm^2)[73] and nanostructured LSC (0.02 Ω cm^2)).[72] Moreover, the MP-LSCF cathode shows a lower activation energy of 0.91 eV, compared with 1.46 eV for the bare one (Figure 8e). The excellent ORR activity also promotes the single-cell power density from around 0.75 to 1.2 W cm^{-2} at 600 °C (Figure 8f).[26]

Anodes for O^{2-}-LT-SOFC: This section focuses on new materials and new microstructure/designs for the anode of LT-SOFC. More comprehensive SOFC anode reviews can be found in refs. [10,67,130,131].

The anode acts as the electrochemical reaction region for fuel oxidization (taking H_2 as example here): $H_2 + O_O^x \rightarrow H_2O + 2e^- + V_O^{\cdot\cdot}$. This process takes via H_2 adsorption on the anode surface, electron, and oxygen ion transfer

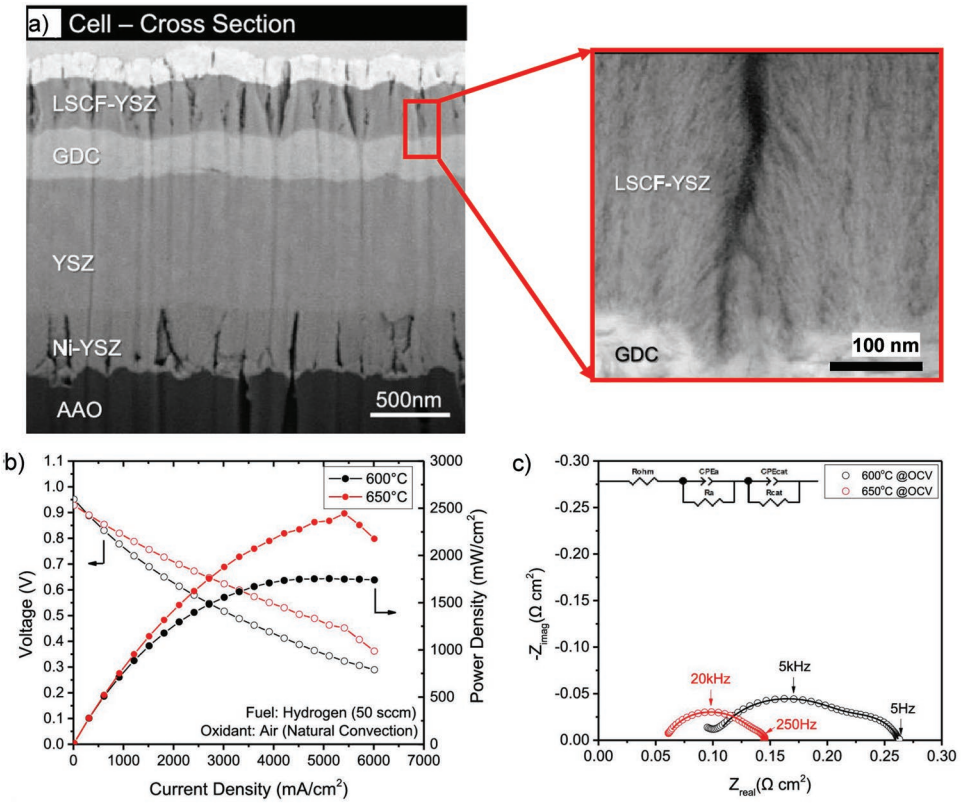

Figure 7. a) Cross-section FE-SEM image of the cell architecture, together with the scanning mode TEM view of the cathode, AAO: anodized aluminum oxide substrate. YSZ: yttria-stabilized zirconia, GDC: gadolinia doped ceria, LSCF: $La_{0.6}Sr_{0.4}Co_{0.2}Fe_{0.8}O_{2.95}$. b) Current–voltage–power curves and c) EIS measurement with hydrogen fuel and air at 600 and 650 °C, respectively. Reproduced with permission.[15] Copyright 2020, American Chemical Society.

over the reaction sites. Like the cathode, the anode must also provide enough reaction sites, sufficient catalytic activity, and adequate ionic and electronic conductivity. The anode of O^{2-}-SOFC is often a composite of the electrolyte material (function as the oxygen ion conductor) and an electronic conductor with catalytic activity for fuel oxidation. Ni is by far the most applied anode material for its unique properties toward hydrocarbons reforming and good electron conductivity.[132–134] Since YSZ is the most applied electrolyte material for conventional SOFCs, Ni-YSZ composite anodes are developed for compatibility.

For high power densities at temperatures around or below 600 °C, the anode performance needs to be improved relative to the one provided by micrometer-sized composite Ni/YSZ electrodes. One effective way to improve the anode performance is the use of materials with higher ionic conductivity than YSZ.[135] Ni-GDC and Ni-SDC are therefore widely used for LT-SOFCs, yielding good performance.[19,27,40,136] For example, a nanoscale Ni-GDC results in an anode resistance of 0.14 Ω cm^2 (GDC as electrolyte and 3% H_2O-H_2 as fuel) at 600 °C.[137] Lee et al. were able to achieve a superior power density of 2 W cm^{-2} at 550 °C for a GDC-based cell (cathode: BSCF-GDC, electrolyte: GDC, anode: Ni-GDC).[40] In addition, an anode composite consisting of Ni and a mixed oxide ionic and protonic phase, with the representative composition of $BaZr_{0.1}Ce_{0.7}Y_{0.2-x}Yb_xO_{3-\delta}$ (BZCYYb), can also be used as anode material for LT-SOFCs with an oxygen ion conductor as electrolyte. When used as an anode for SOFC (with SDC as electrolyte), Ni-BZCYYb showed excellent coking resistance at 750 °C when fueled with propane with 3 vol% H_2O and remarkably also when fueled with H_2 containing 10 ppm of H_2S. This was primarily attributed to the high ionic conductivity and the preferred water absorption capability of BZCYYb to facilitate the oxidation of elemental sulfur.[53,138] Combined with a $Ce_{0.90}Ni_{0.05}Ru_{0.05}O_2$ (CNR) catalyst, a Ni-BZCYYb-based anode composite applied on an SDC electrolyte was shown capable of operating on fairly dry methane (3.5% vol H_2O) at 500 °C. The peak power density reached 0.37 W cm^{-2} (CH_4 with 3.5% vol H_2O) with the CNR coating. The cell also showed good durability, with a constant cell voltage of 0.75 V for a period of 380 h and no obvious coking observed after the cell test. The synergetic catalytic role of the CNR catalyst is suggested to work as follows: some exsoluted Ni atoms facilitate the breaking of the methane C—H bond, and an oxygen vacancy is formed for activating CH_4 to CO; the nearby exsoluted Ru combined with the oxygen vacancy then facilitates the activation of H_2O to produce an oxygen atom to fill the vacancy. To put it in a nutshell, the coking resistance was attributed to the bifunctional catalytic effects of the well-anchored and nanosized Ni and Ru cations on the CeO_2 surface, and the coupling of the dissociated species on the active sites to minimize the coking poisoning effects.[19]

Decreasing the grain size in the anode is another effective way to decrease the anode resistance according to the transmission-line model.[135] For example, Gao et al. theoretically showed that an average grain size of 0.1 μm in the

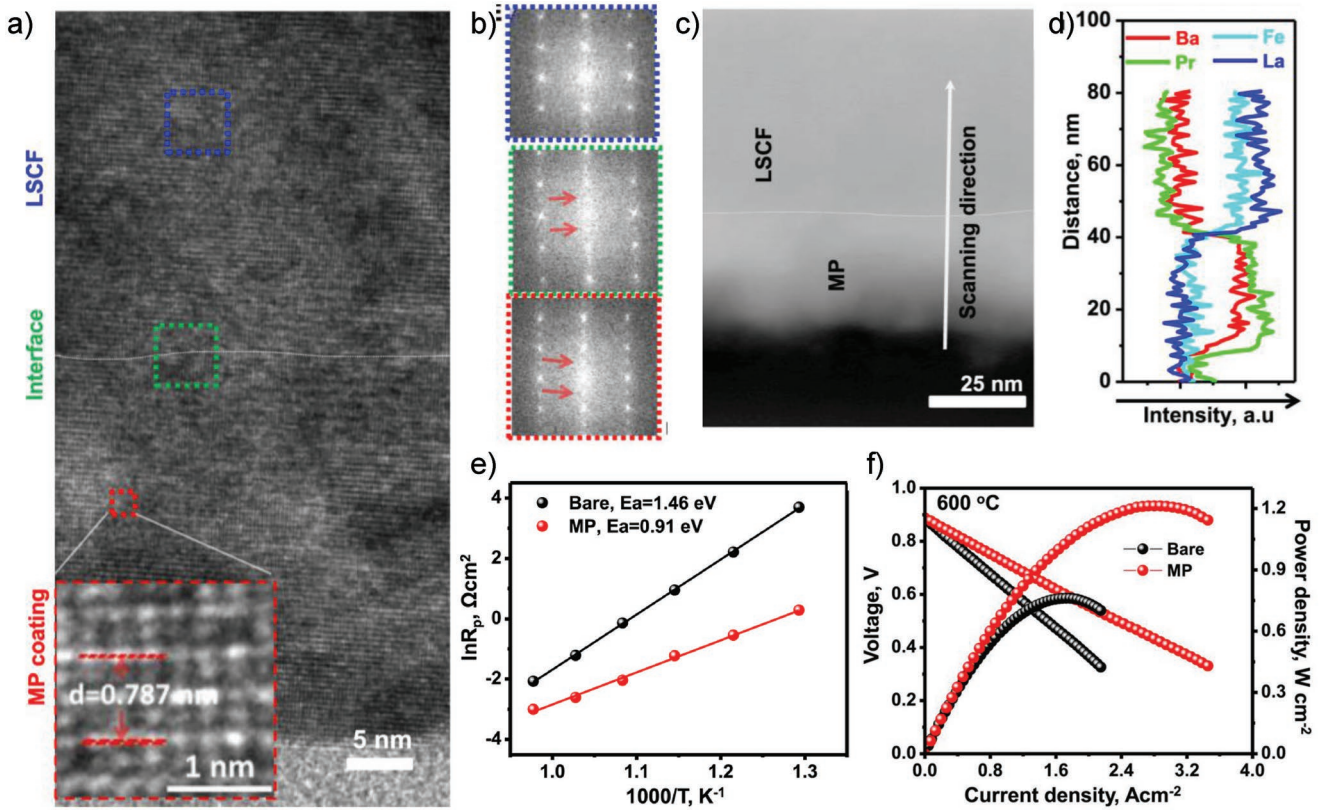

Figure 8. a) Cross-sectional TEM image of MP (multiple phase catalyst, $BaCoO_{3-\delta}$ and $PrCoO_{3-\delta}$ nanoparticles and a conformal $PrBa_{0.8}Ca_{0.2}Co_2O_{5+\delta}$ film)–LSCF interface, b) fast Fourier transform (FFT) patterns of LSCF (blue box), interface (green box), and MP catalyst (red box), the red arrows indicate the double perovskite structure, c,d) typical high-angle annular dark-field scanning transmission electron microscopy (HAADF-STEM) image of MP-LSCF interface, scanned from bottom to top, e) temperature dependence of interfacial polarization resistance (R_p) of bare and MP-coated LSCF cathodes under OCV conditions. f) Typical voltage–current–power curves of Ni-GDC anode-supported cells with bare LSCF and MP catalyst-coated LSCF at 600 °C using H_2 (3 vol% H_2O) as fuel and ambient air as oxidant. LSCF: $La_{0.6}Sr_{0.4}Co_{0.2}Fe_{0.8}O_{3-\delta}$. Reproduced with permission.[26] Copyright 2018, Elsevier Inc.

anode yields an anode resistance smaller than 0.1 Ω cm^2 at 600 °C while much finer anode microstructure, in nanoscale, is needed if aiming for the same resistance at 500 °C.[10] Park et al. recently fabricated two SOFCs with different anode microstructures: one with a nanostructured (average grain size of 100 nm) Ni-YSZ anode (referred to as NS-cell) and the other one with a microscale anode (MS-cell). The direct comparison showed that at 500 °C, the NS-cell reached a peak power density of 0.46 W cm^{-2} while the MS-cell only reached 0.27 W cm^{-2} under the same operating conditions.[17] Because of the difficulty in reliably separating the anode and cathode resistance by impedance technique, the authors did not quantitively show the contribution of the anode resistance, but since the cathode was the same for the two cells, it is fair to ascribe most of the improvement to the modified anode structure—directly showing the potential of performance improvement via nanostructuring

2.1.2. H^+-LT-SOFC or PCFC

Electrolytes for PCFC: Several extensive reviews on PCFCs and PCFC-based materials have been published since the discovery of high-temperature proton conductors.[139–143] Herein, we review the most pertinent advances in proton-conducting electrolyte development on reducing SOFC operating temperature. Proton-conducting electrolytes generally exhibit higher conductivity than the oxygen ion-conducting analogs at low temperatures (e.g., 300–600 °C) due to the lower activation energy for proton conduction. The discovery of proton conduction in $SrCeO_3$-based ceramics at high temperatures (above 600 °C) sparked the interest for protonic ceramic fuel cells.[144] Later Iwahara et al. reported the finding of high proton conduction (around 10^{-2} S cm^{-1} at 600 °C) in Y_2O_3-doped $BaCeO_3$, $BaCe_{0.9}Y_{0.1}O_{3-\delta}$ (BCY), under humidified hydrogen atmosphere.[145] But BCY is chemically unstable in CO_2 and H_2O containing atmosphere below 800 °C ($BaCeO_3 + CO_2 \rightarrow BaCO_3 + CeO_2$).[146–149] Doped barium zirconate, $BaZr_{0.9}Y_{0.1}O_{3-\delta}$ (BZY), shows excellent tolerance to CO_2,[138] but its application is limited by its poor sinterability (required sintering temperatures above 1600 °C)[150–153] and highly resistive grain boundaries.[141,154] The solid solution of barium cerate and barium zirconate, $BaCe_{0.9-x}Zr_xY_{0.1}O_{3-\delta}$ (BCZY), provides an effective composition trade-off between performance and stability: increasing the Ce content improves the conductivity while increasing the Zr content improves the chemical stability.[148,149,154] As such, BCZY has often been

considered a model electrolyte material for PCFC, and efforts have focused on further enhancing its stability and conductivity in the last decades.

In general, the proton conductivity of BCZY can be further enhanced if there are no or fewer blocking effects from the grain boundaries. Pulsed laser deposition (PLD) is a flexible technique capable of fabricating a thin film with a controlled microstructure. Recently, Bae et al. demonstrated the effectiveness of fabricating an ultrathin BCZY ($BaCe_{0.55}Zr_{0.3}Y_{0.15}O_{3-\delta}$) electrolyte film by PLD to enhance the PCFC performance. As shown in the high-magnification SEM image (**Figure 9**a), a high-quality 1 µm BCZY electrolyte film with vertically split and single-grain columnar structure was obtained. Confirmed with the conductivity measurements performed in the in-plane and out-of-plane directions (Figure 9b,c), the resistance was significantly decreased (two orders of magnitudes) for a film with such single-grain columnar microstructure. The very thin grain-boundary free microstructure led to an electrolyte ASR_{el} of 0.07 Ω cm^2 and a power density of 0.8 W cm^{-2} at 550 °C (Figure 9d), much higher than the average power density of other PCFCs with thicker electrolyte (Figure 9e).[18] Another essential milestone work regarding thin electrolyte development for PCFC was published by An et al.; they fabricated a thin (<5 µm) BCZY electrolyte film with a large membrane area (5 × 5 cm^2). After a cosintering with the anode support at 1350 °C for 4 h, a dense BCZY electrolyte layer was obtained by leveraging the sintering effects from a tunned in situ anode shrinkage. The large-area thin-film electrolyte with reduced grain-boundary density along the ion-conducting direction (average grain size > 3.5 µm) led to an ASR_{el} as low as 0.09 Ω cm^2 at 550 °C. This work demonstrates a breakthrough in the scalable fabrication of thin electrolytes for PCFC.[29]

Further efforts to improve the properties of BCZY have focused on tuning the doping on the B-site. A representative composition is the $BaZr_{0.1}Ce_{0.7}Y_{0.1}Yb_{0.1}O_{3-\delta}$ (BZCYYb1711), a mixed H^+ and O^{2-} conductor, characterized by Yang et al.[53] They reported a synergetic effect of Y and Yb, leading to increased ionic conductivity and higher peak power density. Since then, BZCYYb has sparked lots of interest as PCFC electrolyte.[19,31,155–157] However, Choi et al.[14] and Vahid Mohammadi et al.[158] subsequently observed that BZCYYb1711 was not chemically stable under high CO_2 content (10% CO_2 + 90% H_2) due to the high content of cerium. By contrast, they reported a new stoichiometry with a higher Zr content ($BaZr_{0.4}Ce_{0.4}Y_{0.1}Yb_{0.1}O_{3-\delta}$ (BZCYYb4411)) with enhanced chemical tolerance to CO_2. The compromise was a poorer sinterability (1600 °C for 24 h) and decreased conductivity.[14]

Sintering aids (Co, Ni, Zn) have been investigated to enhance the sinterability of BZY and BCZY with high Zr contents.[150,151,159] The sintering temperature was successfully lowered by 100–250 °C, but with minor effects on the conductivity (both bulk and grain-boundary contributions). The discovery of solid-state reactive sintering (SSRS) has been a game-changer in the preparation of thin BCZY supported BCZY/NiO half cells.[160–162]

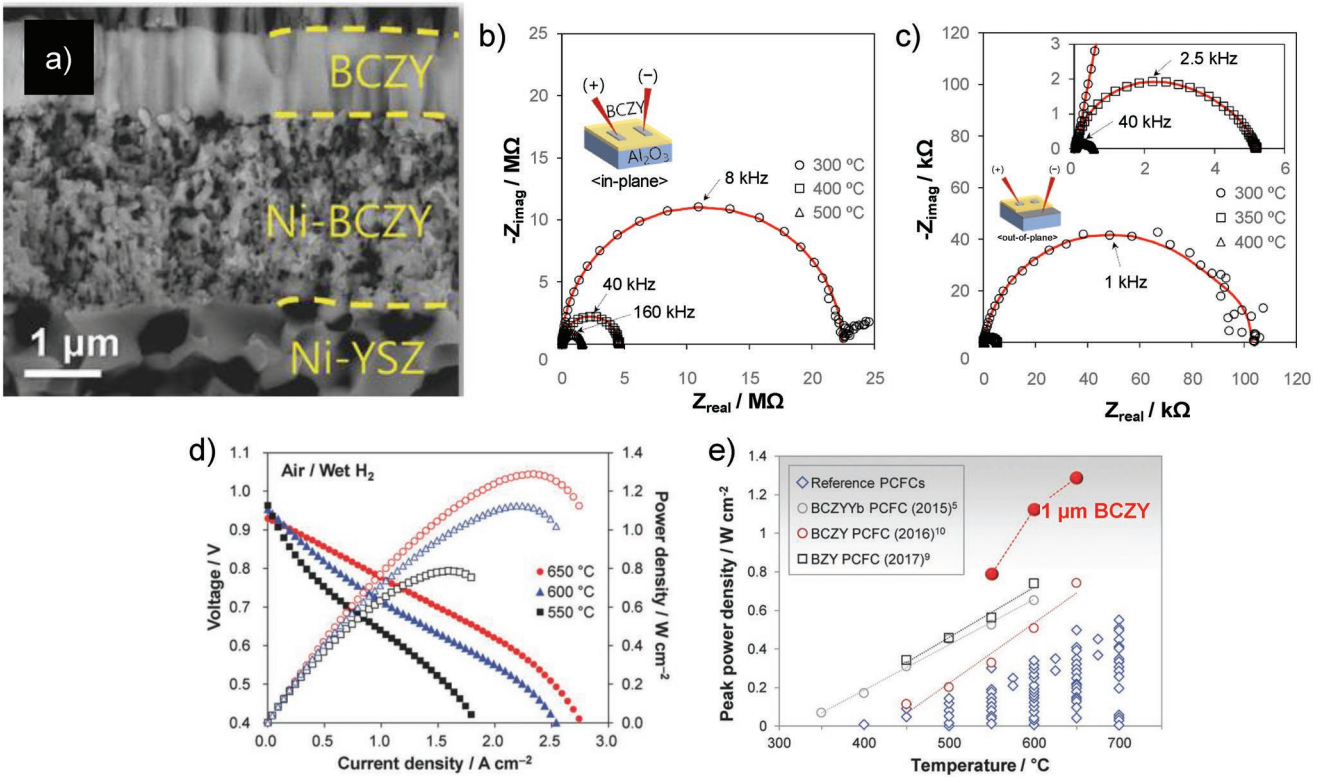

Figure 9. a) SEM images of the sample structure. Nyquist plots of AC impedance spectra obtained from the b) in-plane and c) cross-plane conductivity measurements. d) Cell performance recorded at different temperatures. e) Comparison of peak power densities between the PLD fabricated 1 µm BCZY electrolyte and other PCFCs with thicker electrolytes, BCZY: $BaCe_{0.55}Zr_{0.3}Y_{0.15}O_{3-\delta}$. Reproduced with permission.[18] Copyright 2018, Wiley-VCH GmbH & Co. KGaA, Weinheim.

Contrary to traditional sintering, where the sintering aid is added to the presynthesized powder, SSRS is a single step that combines synthesis and sintering. The precursors are mixed with a small amount of NiO (0.5 to 2 wt%), shaped to the desired form (pressing, tape-casting, extrusion), and sintered at 1400–1500 °C.

To rationally design a proton conductor with both stability and performance, a new perspective may be needed beyond the compromise in tunning the Zr or Ce content. Recently, Murphy et al. reported a new composition with a complete replacement of Zr with a similar-ionic-radius Hf. $BaHf_xCe_{0.8-x}Y_{0.1}Yb_{0.1}O_{3-\delta}$ (x = 0.1–0.3) was found to exhibit better chemical stability and proton conductivity than the BZCYYb, providing a new approach to stabilize the BCZY-based materials.[163]

Cathodes for PCFC: The overall reaction happening at the PCFC cathode is given by reaction (1)

$$\frac{1}{2}O_2 + 2e^- + 2H^+ \rightarrow H_2O \quad (1)$$

The SOFC cathode material requirements of high electronic conductivity and ORR activity are also required by PCFC cathodes. Therefore, the early PCFC cathodes directly utilized the high performance MIEC SOFC cathode materials: $Ba_{0.5}Sr_{0.5}Co_{0.8}Fe_{0.2}O_{3-\delta}$ (BSCF),[29,164,165] $La_{0.6}Sr_{0.4}CoO_{3-\delta}$ (LSC),[18,166] and $La_{0.6}Sr_{0.4}Co_{0.8}Fe_{0.2}O_{3-\delta}$ (LSCF),[167,168] $Sr_{0.5}Sm_{0.5}CoO_{3-\delta}$ (SSC),[169] $BaCo_{0.4}Fe_{0.4}Zr_{0.2}O_{3-\delta}$ (BCFZ),[167] $La_{0.6}Sr_{0.4}Fe_{0.8}Ni_{0.2}O_{3-\delta}$ (LSFN),[164,170] and $PrBa_{0.5}Sr_{0.5}Co_{1.5}Fe_{0.5}O_{5-\delta}$ (PBSCF).[14] The highest power density of a PCFC reported to date is 1.3 W cm^{-2} at 600 °C using a BSCF cathode. However, it rapidly decreased to 0.5 W cm^{-2} at 500 °C,[29] not superior to the performance of LT-SOFCs despite the higher PCFC electrolyte conductivity. The major difference between the cathode reaction in an SOFC and a PCFC is the participation of protons. As a result, the use of an MIEC (O^{2-}/e^-) as PCFC cathodes restricts the electrochemically active sites to the 2D interface between the electrolyte and the cathode. Consequently, cathode materials with additional proton conduction will enhance the PCFC performance by extending the electrochemically active sites beyond the electrolyte/cathode interface (**Figure 10**a). But theoretically, a PCFC (with a proton-conducting electrolyte) cathode with rationally designed 1) surface activity for the ORR and 2) mixed protonic and electronic bulk conductivities should also function well and more efficiently. Figure 10b visually illustrates the possible reaction steps for such a material, significantly expanding the active sites to the whole cathode surface. However, so far, there are not so many reports of such material under oxidizing atmosphere.

Therefore, recent efforts in PCFC cathode development have been devoted to two main routes: mixing conventional MIEC cathodes (O^{2-}/e^-) with proton conductors and seeking to design a single cathode material with triple conducting properties ($O^{2-}/e^-/H^+$). The latter category is referred to as triple conducting oxide (TCO). A couple of reviews focusing on cathode materials for PCFCs are available in literature.[139,171–176] Some examples are highlighted below.

MIEC/proton-conducting ceramic composites can be prepared by mechanical mixing,[177–180] infiltration,[181–184] or exsolution.[185] While the first technique is the easiest, coarse grains are often obtained, with little or no control over the microstructure. Infiltration and exsolution allow for the preparation of electrocatalyst nanoparticles.

Prepared from a single-phase precursor via an oxidation-driven exsolution process, Rioja et al. reported the synthesis of a nano TCO composite, with the nominal composition of $0.6La_{0.5}Ba_{0.5}Co_{1/3}Mn_{1/3}Fe_{1/3}O_{3-\delta}$-$0.4BaZr_{1-x}Y_xO_{3-\delta}$. The tailored composition and microstructure (intimately interconnected nanophases caused by the exsolution) resulted in a low ASR_c of 0.44 Ω cm^2 at 600 °C (3% humid air) for a symmetric cell test.[185] For a similar mechanism, Liang recently reported a high-performance $Ba_{0.95}(Co_{0.4}Fe_{0.4}Zr_{0.1}Y_{0.1})_{0.95}Ni_{0.05}O_{3-\delta}$ cathode. Benefitting from the nanosized NiO exsolution to facilitate surface oxygen exchange processes, its ASRc (0.36 Ω cm^2) can be decreased by nearly half compared to the $Ba(Co_{0.4}Fe_{0.4}Zr_{0.1}Y_{0.1})_{0.95}Ni_{0.05}O_{3-\delta}$ without NiO exsolution (0.57 Ω cm^2) and

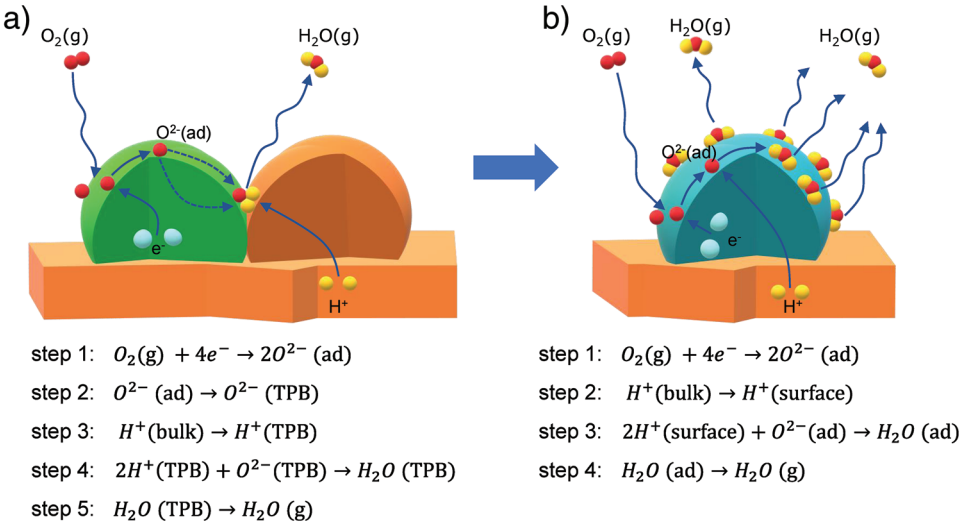

Figure 10. Visualizations of the possible reaction steps for a) cathode composite of MIEC (mixed ionic and electronic conductor) and proton conductor, and b) a rationally designed single phase cathode with surface ORR activities and mixed protonic and electronic bulk conductivities. "ad" represents the "adsorbed" on the surface.

resulted in a 60% cell power density enhancement at 550 °C (1.17 W cm^{-2} vs 0.72 W cm^{-2}).[186] Similarly, Song et al. synthesized a cathode material with the nominal composition of $BaCo_{0.7}(Ce_{0.8}Y_{0.2})_{0.3}O_{3-\delta}$ (BCCY), which was assembled into two homogeneously distributed phases with intimate contact at the nanoscale during calcination. One phase is a Ce-rich phase with a composition close to the proton conductor $BaCe_{0.8}Y_{0.2}O_{3-\delta}$ (BCY), while the other is a Co-rich phase close to the MIEC $BaCoO_{2.23}$.[28] Because of their intimate mixing, their nanostructure and the synergetic effects of ORR ($BaCoO_{2.23}$ contribution) and proton conduction (BCY contribution), a high electrochemical performance was achieved: the oxygen bulk diffusion coefficient (D_{chem}) and surface exchange coefficient (k_{chem}) were about one order of magnitude higher than the well-known BSCF[71] and BCFZY.[31] A peak power density of 0.251 W cm^{-2} was measured at 500 °C when applying the BCCY composite into a single fuel cell. Later, they leveraged this work by making a multiphase consisting of $SrFeO_{3-\delta}$, $SrCeFeNiO_{3-\delta}$ (SCFN), and exsoluted nanosized RP structure phases. With the promoted hydration and proton conductivity caused by the RP phase, an attractive performance of 0.53 W cm^{-2} at 550 °C was obtained.[187] Shi et al. also reported the synergetic effect of a hetero-phase. The nominal composition of $LaSr_{2.7}Co_{1.5}Fe_{1.5}O_{10-\delta}$ was formed by mixing a single perovskite of $LaSr_2Co_{1.5}Fe_{1.5}O_{10-\delta}$ and an RP $LaSr_3Co_{1.5}Fe_{1.5}O_{10-\delta}$ phase. This composition outperformed the single phase in both performance and durability.[188]

The concept of a triple-ion ($O^{2-}/e^-/H^+$) conducting cathode for PCFC was pursued by Kim et al. in 2014. They developed a novel double-layered perovskite material, $NdBa_{0.5}Sr_{0.5}Co_{1.5}Fe_{0.5}O_{5+\delta}$ (NBSCF), purported to facilitate the ions migration through channels between the AO layers of the $AA'B_2O_5$ structure, leading to an outstanding PCFC power density, 0.69 W cm^{-2} at 600 °C.[155] The $PrBa_{0.5}Sr_{0.5}Co_{1.5}Fe_{0.5}O_{5+\delta}$ (PBSCF), a derivative of NBSCF, is another noteworthy cathode material for PCFC because of its higher electronic conductivity compared to NBSCF.[14,19] Choi et al. demonstrated that the electrochemical performance of PBSCF cathode was significantly enhanced compared with the conventional LSCF MIEC cathode. They fabricated two similar PCFCs: one using LSCF and the other using PBSCF as the cathode. The power density increased from 0.2 to over 0.4 W cm^{-2} at 500 °C when switching from LSCF to PBSCF. Additionally, when applying a 100 nm thin PBSCF interlayer between the PBSCF cathode and the electrolyte (**Figure 11**a), the output power density was boosted to higher than 0.5 W cm^{-2} at the same temperature (Figure 11c,d).[14] This interlayer was fabricated by PLD to mitigate the interfacial contact resistance (Figure 11b).

The perovskite $BaCo_{0.4}Fe_{0.4}Zr_{0.1}Y_{0.1}O_{3-\delta}$ (BCFZY), developed by Duan et al., also shows a great PCFC performance at low temperature, 0.65 W cm^{-2} at 600 °C and 0.45 W cm^{-2} at 500 °C.[31] The design strategy of BCFZY is to enhance the electronic conductivity (reaching a range of 1–1.4 S cm^{-1} between 450 and 600 °C) of the well-known proton conductor BZY ($BaZr_xY_{1-x}O_{3-\delta}$) by heavily doping the B-site with the transition-metal cations of Co and Fe. In addition to the MIEC, a double perovskite $BaGd_{0.8}La_{0.2}Co_2O_{6-\delta}$ (BGLC) was recently found to be a good mixed proton and electron conductor below 550 °C, with a proton uptake of 3% at 400 °C and an activation energy of 0.5 eV for the polarization resistance (specifically, 10 Ω cm^2 at 350 °C measured as a symmetric cell in moist atmospheres).[189]

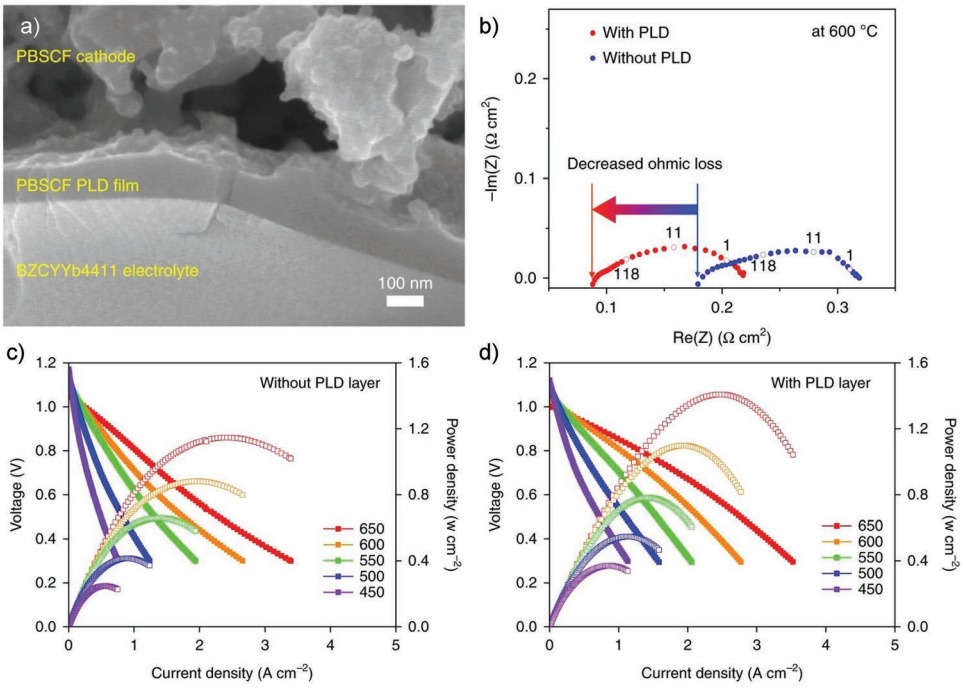

Figure 11. a) Cross-sectional view of the PLD fabricated PBSCF cathode interlayer at the interface between the electrolyte and cathode. b) Comparison for impedance spectra between two identical cells with and without the thin cathode PLD interlayer. c,d) Current–voltage–power density curves comparison between two identical cells with and without the cathode PLD interlayer, PBSCF: $PrBa_{0.5}Sr_{0.5}Co_{1.5}Fe_{0.5}O_{5+\delta}$. Reproduced with permission.[14] Copyright 2018, Springer Nature.

With further microstructural optimization, BGLC could have great potential to be used as a PCFC cathode.

Even though numerous PCFC cathode materials have been synthesized and investigated, some uncertainty on the best routes for further optimization still remains. Further work in the following areas is important.

1) Promising cathode materials from the double-perovskite family have been studied. While the oxygen ions (and not the protons) determine the overall ionic conductivity in $PrBaCo_2O_{5+\delta}$,[190] the opposite trend is reported for $Ba_{0.5}Gd_{0.8}La_{0.7}Co_2O_{6-\delta}$ (BGLC).[189,191]
2) For mixed conducting cathode materials, a proton conductivity of 10^{-5} S cm^{-1} should be sufficient for the surface ORR.[192] However, it is experimentally challenging to measure the protonic conduction in a material that exhibits electronic and/or oxygen ion conductivities of several orders of magnitude higher.[171] Therefore, more work on method development and applying existing methods to pinpoint the absolute level of the minority conductivity would be fruitful to explain behavior and direct further optimization.
3) It is difficult to maximize the electronic and protonic conductivities simultaneously because of the interaction between the electronic and protonic defects in the materials.[172] Therefore, further research is needed to identify compositions that compromise well between optimal electronic and protonic conductivity.
4) The electronic conductivity through the electrolyte affects the determination of the cathode ASR. Therefore the comparison between various cathode materials is challenging. This issue is well addressed by Strandbakke et al.[189] However, the experimental procedure pointed to in that paper is time- and labor-intensive. The development of protocols enabling a sound comparison will be helpful.
5) Designing experiments (e.g., "in operando" studies) that allow the determination of the rate determination step of the electrode reaction would resolve the current uncertainties on the electrode mechanism.[139,171]

Anodes for PCFC: The PCFC anode development is still in its infancy. Typically, PCFC anode materials should be mixed protonic and electronic conductors and electrocatalytically active for fuel reduction. The PCFC anode design follows the same design principles as applied for SOFC anode materials: a composite made of Ni (acting as electronic conductor and fuel catalyst) and a proton conductor (usually the same composition as the electrolyte for better compatibility). The common anode composites reported so far for PCFCs are of Ni/BZY,[31,193] Ni/BCZY,[18,28,29,31,194] and Ni/BZCYYb.[14,28,31,53,163,195,196] As for SOFC anodes, it is crucial to maximize the TPB area to decrease the PCFC anode resistance. Therefore, it is important to tailor the microstructure of the PCFC anode: porosity, pore size, particle size, and phase volume fractions.[18] In addition, the degradation behavior of the anode also greatly influences the long-term stability of the cell. The degradation is affected by possible coking, contaminant poisoning, and catalyst agglomeration, even though the latter is expectedly less pronounced than for SOFC anodes due to the lower operating temperatures. Duan et al. reported on the presence of exsolved Ni nanoparticles in BZY/Ni PCFC anode prepared by solid-state reactive sintering.[138] When exposed to reducing conditions, a PCFC operating in the 500–600 °C temperature range can trigger the exsolution of Ni nanoparticles (10–100 nm). The cell showed excellent performance and exceptional durability for over 6000 h when directly used with hydrocarbon fuels, providing a novel anode route design for the PCFC under harsh environments.

In addition to supplying the electronic conductivity, Ni also provides porosity in the anode upon the reduction of NiO. Most of the studies use between 40 and 60 wt% of NiO. Onishi et al. prepared BZY20/Ni anodes varying the amount of NiO and recommend using less than 70 wt% NiO in the BZY20/NiO supports.[197] Indeed, cosintered cells with 80 wt% NiO failed due to the mismatch of the thermal expansion coefficients. A stability study of Ni-$BaCe_{0.8}Y_{0.2}O_{3-d}$ (Ni-BCY) and Ni-$BaCe_{0.6}Zr_{0.2}Y_{0.2}O_{3-d}$ (Ni-BCZY) upon redox cycles showed that NiO particles bond more strongly with BCZY than BCY particles.[198]

However, a negative effect of NiO can be observed on the BZY electrolyte performance upon cosintering at high temperatures (1500 °C): Ni is prone to segregate to the BZY electrolyte, extracting the yttrium from BZY to form a secondary phase of BaY_2NiO_5, and the resulted yttrium deficiency in the BZY electrolyte leads to a conductivity loss.[199,200] Therefore, the Ni-cermet effects on BZY-based proton-conductors during cosintering should be thoroughly studied in terms of chemical stability.

2.2. LT-SOFC with μSOFC

Besides the LT-SOFCs developed based on the classic ceramic SOFCs with key components within micrometer scale, another important branch of LT-SOFCs is μSOFC, which is initially designed as battery replacement applications in small electronic devices, such as laptops. Hence, its operating temperature must be kept low, preferably below 500 °C.[201–204] With a similar principle to that of conventional SOFC, much thinner electrolytes (sub-micrometer scale) are used. The latter are generally designed and microfabricated on silicon-based substrates using MEMS-technology-related (microelectromechanical systems) microfabrication techniques. **Figure 12**a illustrates the most studied μSOFC architecture, with a freestanding membrane on a silicon wafer. The overall design of such a μSOFC is achieved by standard microtechnology processes such as sputtering, lithography, and etching.[205] Since the active area of a single μSOFC unit-cell would only be in the range of a few $\approx 100 \times 100$ μm^2 (Figure 12b,c), power output is increased by combining several unit-cells in a patterned arrangement on a larger wafer (Figure 12d).

Figure 13 summarizes the peak power density as a function of temperature for the most investigated μSOFCs configurations. The best performance to date (also the most widely studied) is measured on YSZ electrolyte with Pt electrodes. However, these systems show poor reliability and insufficient lifetime (less than a few tens of hours[34,207]) because of the Pt microstructural instability and the ultra-thin YSZ electrolyte mechanical fragility. It is therefore needed to develop new designs and alternative materials. Here, perovskite-type oxides for the cathode, nonprecious metals for the anode, and possible proton conductors for the electrolyte are interesting options.

As already mentioned in Section 2.1.2, proton conductors exhibit lower activation energy for ion conduction than oxygen-ion conductors.[141] Therefore, μSOFCs with proton-conducting

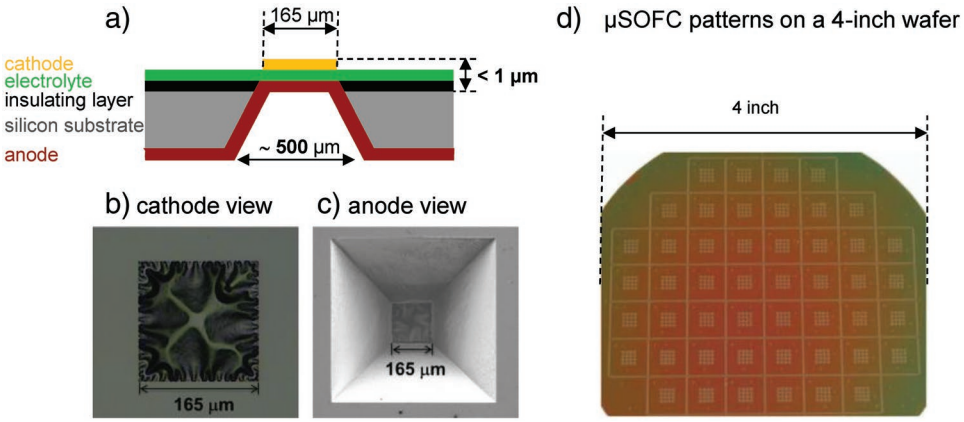

Figure 12. a) Scheme of a freestanding µSOFC membrane on a silicon substrate and microscopy images of the µSOFC seen from b) cathode side and c) anode side (the dimension value is given as an example). d) optical image of 832 individual µSOFCs patterned on a 4 in. wafer. (a–c) Reproduced with permission.[206] Copyright 2014, Elsevier B.V. (d) Reproduced with permission.[205] Copyright 2006, The Electrochemical Society.

electrolytes could achieve a higher performance at 500 °C than those with O^{2-} conducting electrolytes. However, to date, the highest performance of a µSOFC with a proton conductor (marked in red open star in Figure 13) is lower than the performance reached with oxide ion-conducting µSOFCs. For example, a Pt/YSZ/Pt and a Pt/BZY/Pt (with similar dimensions and testing conditions) exhibited a peak power density at 400 °C of 0.437 and 0.076 mW cm^{-2}, respectively.[37] Since the research of proton-conducting µSOFC is still in its infancy with only a few studies, the following section focuses on oxide ion-conducting µSOFCs.

Electrolytes for O^{2-}-µSOFC: As evident from the data summarized in Figure 13, YSZ is the most widely used electrolyte material for µSOFC.[205,218,219] Because of the resistance increase at lower operating temperatures, the thickness of the YSZ layer must be below a few hundred nanometers to reach attractive power densities (for example, assuming a polarization voltage of 0.5 V, a 200 nm YSZ electrolyte can theoretically achieve ≈1.5 W cm^{-2} at 500 °C[1,220]). It is challenging to prepare such a thin pinhole-free layer, especially when deposited by vapor deposition techniques such as PLD. The thin films often grow with a columnar structure under high vacuum deposition pressure (in most cases lower than 10^{-2} mbar),[125,114] facilitating undesirable gas diffusion in the minor gaps between the grains.[54,222] Gas leakage is observed with OCVs lower than 1 V for YSZ-based µSOFC[36,207,218] when tested in nearly pure dry H_2 (with 3 vol% humidity). It is also challenging to achieve the required footprint with cell areas in the hundreds of mm^2 range: large-area and thin membranes are susceptible to buckling failure. The critical compressive stress σ_{cr} at which buckling occurs in a membrane can be given by $\sigma_{cr} = -1.22\frac{E}{1-\nu^2}\left(\frac{h}{b}\right)^2$, where E is the Young's modulus, ν is the Poisson ratio, h and b are the thickness and area of the membrane, respectively.[223]

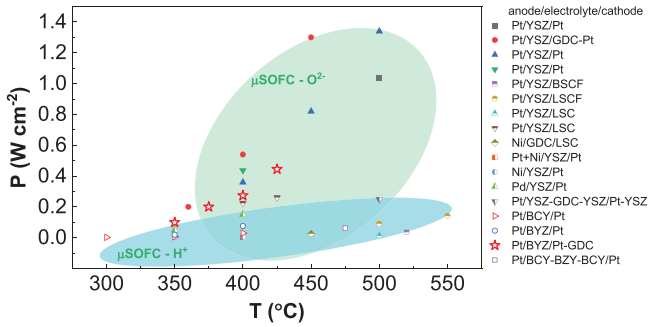

Figure 13. Comparison of peak power density for µSOFC with different materials, with reference in legend from top to bottom.[33–37,206,208–217] LSC (lanthanum strontium cobaltite), LSCF (lanthanum strontium cobalt ferrite), BSCF (barium strontium cobalt ferrite), BCY (yttrium-doped barium cerates), and BZY (yttrium-doped barium zirconates).

An et al. demonstrated a high-performance µSOFC with a pinhole-free YSZ electrolyte and increased active area through a corrugating structure (**Figure 14**a,b). They grew a conformal 50 nm thin YSZ on a corrugated template (nitride) by atomic layer deposition (ALD) and nanosphere lithography. The ultrathin electrolyte layer with an enhanced effective area (caused by the 3D architecture) led to an ohmic resistance lower than 0.1 Ω cm^2 at 450 °C (Figure 14c), together with an OCV of 1.06 V and a peak power density of 1.3 W cm^{-2} (Figure 14d). It corresponds to an enhancement close to a factor 2 compared with a similar cell without the 3D structure.[35] Tsuchiya et al. fabricated a 54 nm thin YSZ electrolyte with an enhanced lateral dimension (over 10 mm^2) on a metallic grid.[207] It is important to note that this latter work was on a planar structure. Despite a power density of only 0.1 W cm^{-2} at 450 °C (LSCF was used as the cathode), the absolute power output was increased by a factor of seven, attributed to the increased area utilization for a single membrane area.

Reports on µSOFC using O^{2-} conducting electrolytes with higher conductivity than YSZ are rare. To the best of our knowledge, the only other studied example is GDC.[212,216] The performance is comparable to that of a YSZ-µSOFC (peak power density of 0.25 W cm^{-2} at 500 °C for a 300 nm GDC electrolyte), even though GDC has a higher conductivity than YSZ.[216] By a direct comparison between the microfabrication process for freestanding YSZ and GDC membranes on a silicon-nitride platform, Baertsch et al. found that a GDC membrane was less resistant to fracture than YSZ.[224] Overall, when switching from YSZ to GDC, the benefit of increased conductivity does not

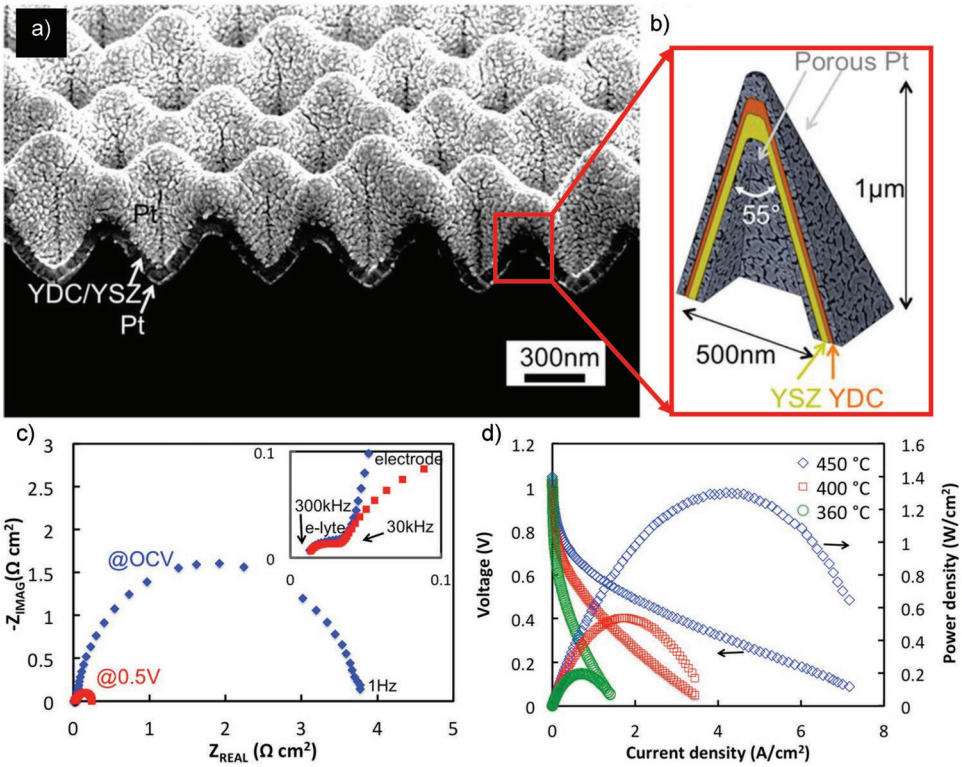

Figure 14. a) 45° tilted view of the cross-section of a 3D freestanding membrane (Pt/YDC/YSZ/Pt), YDC: yttria-doped ceria. b) the schematic of the cross-section of a single pyramid structure and c) impedance spectra of the 3D structured μSOFC recorded at 450 °C at OCV (blue diamond dots) and 0.5 V and d) cell voltage–current–power curves at 450, 400, and 360 °C. Reproduced with permission.[35] Copyright 2013, American Chemical Society.

outweigh the problems associated with the inferior mechanical properties of GDC.

Cathodes for O^{2-}-μSOFC: As shown in Figure 13, Pt is the most studied μSOFC cathode[36,208,222,225,226] because of its catalytic activity toward the ORR at low temperatures (below 500 °C). The major drawback of Pt is its tendency to agglomerate under elevated temperatures. The morphological instability reduces the gas exchange and the adhesion at the cathode/electrolyte interface and impedes the performance and long-term stability.[35,36,226,227] To highlight one example, the power density of the previously discussed high-performance 3D μSOFC with Pt cathode decreases by 30% after a 1 h operation at 400 °C.[35]

Chang et al. found that Pt does not show significant agglomeration when operating at 500 °C under a bias of 0.6 V for 8 h when ALD coated with an ultrathin YSZ layer (5 nm). However, the thickness of the coated YSZ layer must be deliberately tuned to avoid the complete blocking of the active Pt surface. The authors reported that the power density decreased when the thickness of the coated YSZ reached 10 nm.[216] The morphologically more stable MIEC oxides, such as BSCF,[209] LSCF,[207,210,228] LSM,[229] and LSC,[34,211] have been employed in μSOFC to replace the precious Pt metal. But so far, the performance of the μSOFCs with traditional MIEC oxide cathode is lower than that with Pt cathodes because of the inferior activity toward oxygen reduction at temperatures below 500 °C. Evans et al. reported a power density of 0.012 W cm^{-2} at 500 °C for a μSOFC using an LSC cathode.[211] Similar poor performance can also be measured when applying a BSCF cathode, with only 0.035 W cm^{-2} at 520 °C.[209] Evans et al. later reported a μSOFC with a partially amorphous LSC cathode layer grown by PLD (**Figure 15**) that delivered a power density of 0.2 W cm^{-2} at 400 °C, the highest among all the μSOFCs employing MIEC cathodes. The ASR_c of 0.3 Ω cm^2 at 400 °C for the partially amorphous LSC is significantly lower than the best reported value of 2 Ω cm^2 for a crystallized LSC at the same temperature.[230,231] In an in-depth analysis from Cavallaro et al.,[232] a fully amorphous LSC layer obtained by PLD below 400 °C showed a four-time increase of the oxygen diffusion coefficient

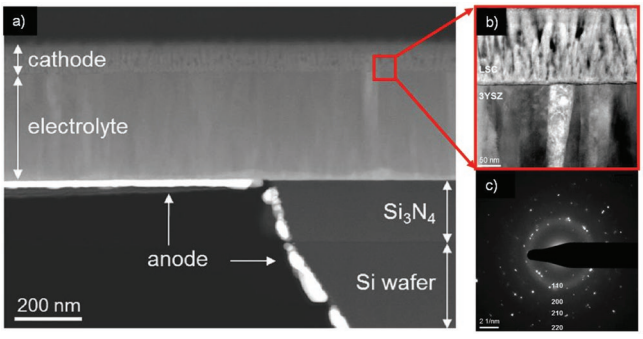

Figure 15. a) Focused ion beam (FIB) cross-section of a freestanding μSOFC. b) High-angle annular dark field scanning transmission electron microscopy (HAADF-STEM) cross-sectional microscopy image of the LSC/YSZ interface. c) Selected area electron diffraction (SAED) pattern of the LSC and parts of the protective carbon cap, LSC: $La_{0.6}Sr_{0.4}CoO_{3-\delta}$. Reproduced with permission.[34] Copyright 2014, Wiley-VCH GmbH & Co. KGaA, Weinheim.

with respect to the crystalline materials and enhanced surface exchange coefficient at 400 °C. The authors did not detect surface chemical composition change for the amorphous layer but a reduction of the activation energy for the oxygen vacancy diffusion. Therefore, the performance enhancement of the amorphous cathode at low temperature was claimed to be caused by the decrease of the energy barrier for the oxygen diffusion. However, this performance enhancement could also be attributed to the associated microstructure change. Low-temperature PLD deposition often leads to nanoporous thin films (Figure 15b),[233] an effective structure allowing for the rapid surface reaction because of the significantly increased TPB.[15,40,72] In other words, the potentially possible nanoporous structure of the amorphous cathode leads to a much larger surface reaction area than the cross-sectional (in parallel to the electrolyte surface) geometrical area. As the ASR_c equals the measured resistance times by the reaction area, an underestimation of the reaction area results in a much smaller ASR_c. For example, Januscheswky et al. showed that an amorphous LSC layer deposited at intermediate temperatures (between 340 and 510 °C) had the lowest resistance compared to the one deposited at room temperature and high temperature of 630 °C.[234] The difference could be explained by the better balance of crystallization and nanoporous structure for the film deposited at intermediate temperatures.[233] The concept of an amorphous cathode shows great potential to enhance the performance at low temperatures, but more systematic studies are needed to understand the physical origin of the enhancement: is it caused by the microstructure, the amorphous state or both?

Anodes for O^{2-}-μSOFC: As shown in Figure 13, Pt is also the most frequently studied anode material for μSOFC.[36,208,222,226,228] Similar to the cathode, the agglomeration at elevated temperatures leads to the anode performance decay. For instance, the cell performance of the previously discussed μSOFC with partially amorphous LSC cathode was limited by the Pt anode agglomeration over time.[34] Wang et al. investigated the thermal stability of a Pt–Ni ($Pt_{0.84}Ni_{0.16}$) anode composite. They found that the power density of the cell with a pure Pt anode continuously decreased (20% loss) when operated at 0.4 V and 400 °C, while the performance of another cell with a Pt–Ni anode was stable (but only for a short observation time of 70 min).[213] Pure metallic Ni has also been investigated by Joo and Choi[212] and Kang[214] et al.: it has sufficient catalytic activity at low temperature but suffers from thermal agglomeration and TEC mismatch with electrolyte materials. Therefore, as for conventional SOFCs, composites made of Ni and a ceramic material should be used as μSOFC anodes. Other precious metals such as ruthenium (Ru) and palladium (Pd) have also been integrated into μSOFCs to investigate their ability to catalyze conversion of hydrocarbons at low temperatures.[215,235,236] Takaki et al. reported a peak power density of 0.45 W cm^{-2} at 500 °C with a Ru-anode-based μSOFC when using CH_4 as fuel, with no carbon deposition after fuel cell test. Moreover, they found that a Ru anode is morphologically more stable under methane than under hydrogen.[215] The potential applications of μSOFCs are where they could supersede batteries because of the higher volumetric power density. This relies on use of liquid fuel with high energy density, and hence it is important to develop electrodes that can operate on syngas and preferably also hydrocarbons to advance this field.

3. Summary

During the last decade, steady progress in developing low-temperature SOFCs to operate below 600 °C has been made. To accelerate the development of practical devices and enhance the performance and stability over time, recent highlights, primary challenges, effective strategies, new directions, and future perspectives have been summarized below.

3.1. Recent Highlights

Encouragingly, some important milestones have been achieved. For example, through a modified solid-state reactive sintering synthesis process, Duan et al. fabricated a PCFC prototype that demonstrated notable performance (0.45 W cm^{-2} at 500 °C under H_2) and durability (degradation rate of less than 1.5%/1000 h for 6000 h test under 11 different fuels).[31,138] This breakthrough sparked a lot of interest in the research community, and many reports of fabrication, upscaling, and testing of PCFCs have followed. An et al. developed a scalable PCFC with outstanding performance (1.3 W cm^{-2}) at 600 °C.[29] While for the oxygen-ion conducting SOFC, a notable breakthrough is a cell enabling the internal methane reforming at 500 °C.[19] Compared to the ceramic fuel cells, the silicon-based μSOFC has been getting less attention, however, a world-record power density (1.3 W cm^{-2}) at 450 °C achieved on a μSOFC with corrugated structure is inspiring the research in this direction.[35]

3.2. Primary Challenges

Despite these encouraging accomplishments, some key challenges remain to be solved. The fundamental mechanisms of the gas/solid interfacial processes have not yet been fully understood. It has been known for years that the overall oxygen exchange reaction is kinetically limiting, but an atomic and molecule-level understanding of the elementary steps and key intermediates involved remains unclear. Characterization techniques that can easily separate the contributions from the different charge carriers are in demand. For example, it is challenging to isolate the effects of protonic conductivity in triple conducting oxide cathode materials, where the ionic (oxygen ions) and electronic contributions to the total conductivity are much higher.

The technical challenges mainly lie in achieving high performance and stability while keeping the cost as low as possible. The goal is to fabricate large cells (a few tens of cm^2) with a thin gas-tight electrolyte with low grain boundary resistance. Regardless of the nature of the electrolyte conduction mechanism (proton vs oxygen-ion conduction), the film thickness should be below ≈5 μm to reach high-performance below 600 °C.

3.3. Possible Strategies Involving Machine Learning (ML)

The sole trial-and-error experimental approach for material design is time-consuming, especially considering the material becomes more complex with increasing the number of dopants and the combination of different structures in multi-component systems. In this regard, the emerging ML offers some hope

through an accelerated process to have a breakthrough on the materials side.[237,238] As a first step, the material design strategy should begin from theoretical insights identifying effective descriptors such as "the oxygen p-band theory,"[66,239] degree of e_g-filling on the transition metals in the electrode,[97] or acidity of dopants (compared to host material).[240] Next, based on these descriptors, DFT studies are desired for proposing novel materials with specific elements and structures. Finally, additional experimental efforts are needed to develop quantitative, reproducible, and faster characterizations. For example, using some in situ capable techniques to capture the charge transfer[127,241] or real-time electrochemistry measurement during the precise control of material creation at the atomic level.[114]

3.4. New Directions

One new direction in oxygen ion-conducting LT-SOFC research is the transition from thin ZrO_2-based electrolytes to multilayered CeO_2-based thin electrolytes. The benefit is evidenced by the improved electrolyte performance when approaching an operation temperature below 600 °C (Figure 4). Single perovskite-structured oxides are still the prevailing oxygen electrode. Further improvements are heading toward increasing the catalytically active sites through nano engineering or the creation of a heterostructure with other oxides. The results from Pr-based oxides or RP oxides look especially promising.

Ni plays an essential role in fuel electrodes but is sensitive to sulfur and carbon precipitation. Therefore, a growing trend is to replace nickel or use an extremely small amount of it, like the well-anchored Ni exsolved from the oxide basis.

PCFC has sparked considerable interest because the protonic conductivity exceeds the oxide ion one in the state of the art oxides in the temperature range between 400 and 600 °C. R&D efforts to decrease the grain boundary electrolyte resistance is currently an active research direction. For example, high-quality membranes could be prepared with the modified solid-state reactive sintering[31] or ceramic processes with the aid of electrode-assisted cosintering effects.[29] To maximize the performance, the cathode development has shifted from the single MIEC to composite materials made of an MIEC and a proton conductor, or a single TCO, which can simultaneously conduct the electron alongside the protons and oxygen ions.[28,79,171]

μSOFC has proved its potential with high power densities for ultrathin electrolytes with noble metal electrodes. Current trends in this area focus on 1) improving the stability of the ultrathin electrolyte via corrugated membrane structures and 2) replacing the noble metal electrodes with high-performance oxides or alloying the noble materials with Ni to reduce the amount of noble metal used.

3.5. Future Perspectives

SOFCs could outshine Li-ion batteries in terms of shorter downtime due to faster charging (refuel within seconds) and higher energy density. Therefore, in the future, low-temperature SOFCs can play a significant role in application areas competing with Li-ion batteries as an alternative power supply source for some portable devices like robots or consumer drones. We propose a new direction of low-temperature SOFC—combining the advantages of all the three types of SOFC discussed in this review—a "miniaturized" (≈1 cm × 1 cm) protonic ceramic fuel cell (mPCFC). High performance mPCFC could be envisioned integrating the established thin-film fabrication techniques from μSOFC, the material/structure solutions that have already shown promising from LT-SOFC, and the proton conductor from PCFC (**Figure 16**). Realizing such an mPCFC module,

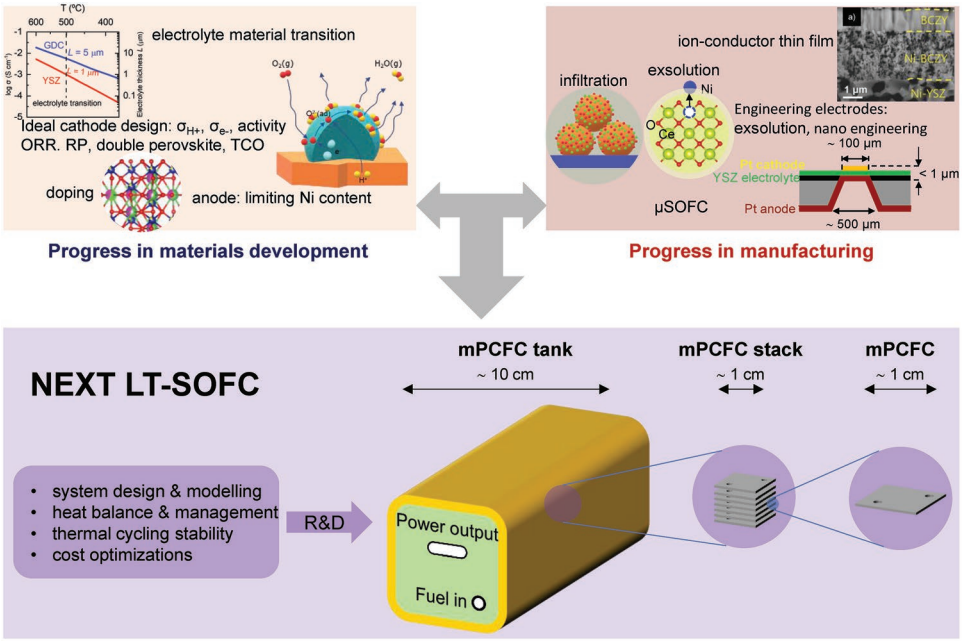

Figure 16. Strategies for the next generation LT-SOFC: miniaturized protonic ceramic fuel cell (mPCFC).

even if benefiting from the achievements within SOFC, will require a significant R&D effort into detailed system design and modeling, heat balance and management, thermal cycling stability, and cost optimizations.

Acknowledgements

The authors acknowledge the financial support from the European Union's H2020-FETPROACT (Grant No. 824072), the support from the Independent Research Fund Denmark (Grant No. 9041-00034B), and the Colorado School of Mines Foundation.

Conflict of Interest

The authors declare no conflict of interest.

Keywords

µSOFC, cathodes, electrolytes, low-temperature SOFC, protonic ceramic fuel cells

Received: November 4, 2021
Revised: February 6, 2022
Published online: March 4, 2022

[1] B. C. H. Steele, A. Heinzel, *Nature* **2001**, *414*, 345.
[2] E. D. Wachsman, K. T. Lee, *Science* **2011**, *334*, 935.
[3] N. Q. Minh, *J. Am. Ceram. Soc.* **1993**, *76*, 563.
[4] A. Hauch, R. Küngas, P. Blennow, A. B. Hansen, J. B. Hansen, B. V. Mathiesen, M. B. Mogensen, *Science* **2020**, *370*, 6118.
[5] Y. Kobayashi, Y. Ando, T. Kabata, M. Nishiura, K. Tomida, N. Matake, *Mitsubishi Heavy Industries Tech. Rev.* **2011**, *48*, 9.
[6] J. Palsson, A. Selimovic, L. Sjunnesson, *J. Power Sources* **2000**, *86*, 442.
[7] F. Han, R. Mücke, T. van Gestel, A. Leonide, N. H. Menzler, H. P. Buchkremer, D. Stöver, *J. Power Sources* **2012**, *218*, 157.
[8] L. Blum, Q. Fang, L. G. J. de Haart, J. Malzbender, N. Margaritis, N. H. Menzler, R. Peters, *ECS Trans.* **2019**, *91*, 2443.
[9] N. Margaritis, L. Blum, P. Batfalsky, D. Bohmann, S. Ceschini, Q. Fang, D. Federmann, J. Kroemer, R. Peters, R. Steinberger-Wilckens, *ECS Trans.* **2015**, *68*, 209.
[10] Z. Gao, L. V. Mogni, E. C. Miller, J. G. Railsback, S. A. Barnett, *Energy Environ. Sci.* **2016**, *9*, 1602.
[11] J. A. Kilner, M. Burriel, *Annu. Rev. Mater. Res.* **2014**, *44*, 365.
[12] D. J. L. Brett, A. Atkinson, N. P. Brandon, S. J. Skinner, *Chem. Soc. Rev.* **2008**, *37*, 1568.
[13] Y. Zhang, R. Knibbe, J. Sunarso, Y. Zhong, W. Zhou, Z. Shao, Z. Zhu, *Adv. Mater.* **2017**, *29*, 1700132.
[14] S. Choi, C. J. Kucharczyk, Y. Liang, X. Zhang, I. Takeuchi, H. il Ji, S. M. Haile, *Nat. Energy* **2018**, *3*, 202.
[15] Y. H. Lee, H. Ren, E. A. Wu, E. E. Fullerton, Y. S. Meng, N. Q. Minh, *Nano Lett.* **2020**, *20*, 2943.
[16] E. O. Oh, C. M. Whang, Y. R. Lee, S. Y. Park, D. H. Prasad, K. J. Yoon, J. W. Son, J. H. Lee, H. W. Lee, *Adv. Mater.* **2012**, *24*, 3373.
[17] J. H. Park, S. M. Han, K. J. Yoon, H. Kim, J. Hong, B. K. Kim, J. H. Lee, J. W. Son, *J. Power Sources* **2016**, *315*, 324.
[18] K. Bae, D. H. Kim, H. J. Choi, J. W. Son, J. H. Shim, *Adv. Energy Mater.* **2018**, *8*, 1801315.
[19] Y. Chen, B. DeGlee, Y. Tang, Z. Wang, B. Zhao, Y. Wei, L. Zhang, S. Yoo, K. Pei, J. H. Kim, Y. Ding, P. Hu, F. F. Tao, M. Liu, *Nat. Energy* **2018**, *3*, 1042.
[20] S. S. Shin, J. H. Kim, K. T. Bae, K.-T. Lee, S. M. Kim, J.-W. Son, M. Choi, H. Kim, *Energy Environ. Sci.* **2020**, *13*, 3459.
[21] J. H. Kim, J. K. Kim, H. G. Seo, D. K. Lim, S. J. Jeong, J. Seo, J. Kim, W. C. Jung, *Adv. Funct. Mater.* **2020**, *30*, 2001326.
[22] Y. Song, Y. Chen, M. Xu, W. Wang, Y. Zhang, G. Yang, R. Ran, W. Zhou, Z. Shao, *Adv. Mater.* **2020**, *32*, 1906979.
[23] B. K. Park, S. A. Barnett, *J. Mater. Chem. A* **2020**, *8*, 11626.
[24] X. Kuai, G. Yang, Y. Chen, H. Sun, J. Dai, Y. Song, R. Ran, W. Wang, W. Zhou, Z. Shao, *Adv. Energy Mater.* **2019**, *9*, 1902384.
[25] Y. Chen, S. Yoo, Y. Choi, J. H. Kim, Y. Ding, K. Pei, R. Murphy, Y. Zhang, B. Zhao, W. Zhang, H. Chen, Y. Chen, W. Yuan, C. Yang, M. Liu, *Energy Environ. Sci.* **2018**, *11*, 2458.
[26] Y. Chen, Y. Choi, S. Yoo, Y. Ding, R. Yan, K. Pei, C. Qu, L. Zhang, I. Chang, B. Zhao, Y. Zhang, H. Chen, Y. Chen, C. Yang, B. deGlee, R. Murphy, J. Liu, M. Liu, *Joule* **2018**, *2*, 938.
[27] M. Li, M. Zhao, F. Li, W. Zhou, V. K. Peterson, X. Xu, Z. Shao, I. Gentle, Z. Zhu, *Nat. Commun.* **2017**, *8*, 13990.
[28] Y. Song, Y. Chen, W. Wang, C. Zhou, Y. Zhong, G. Yang, W. Zhou, M. Liu, Z. Shao, *Joule* **2019**, *3*, 2842.
[29] H. An, H. W. Lee, B. K. Kim, J. W. Son, K. J. Yoon, H. Kim, D. Shin, H. il Ji, J. H. Lee, *Nat. Energy* **2018**, *3*, 870.
[30] K. Bae, D. Y. Jang, H. J. Choi, D. Kim, J. Hong, B. K. Kim, J. H. Lee, J. W. Son, J. H. Shim, *Nat. Commun.* **2017**, *8*, 14553.
[31] C. Duan, J. Tong, M. Shang, S. Nikodemski, M. Sanders, S. Ricote, A. Almansoori, R. OHayre, *Science* **2015**, *349*, 1321.
[32] M. Liang, F. He, C. Zhou, Y. Chen, R. Ran, G. Yang, W. Zhou, Z. Shao, *Chem. Eng. J.* **2020**, *420*, 127717.
[33] Y. Li, S. Wang, P. C. Su, *Sci. Rep.* **2016**, *6*, 22369.
[34] A. Evans, J. Martynczuk, D. Stender, C. W. Schneider, T. Lippert, M. Prestat, *Adv. Energy Mater.* **2015**, *5*, 1400747.
[35] J. An, Y.-B. Kim, J. Park, T. M. Gür, F. B. Prinz, *Nano Lett.* **2013**, *13*, 4551.
[36] K. Kerman, B. K. Lai, S. Ramanathan, *J. Power Sources* **2011**, *196*, 2608.
[37] J. D. Baek, Y. J. Yoon, W. Lee, P. C. Su, *Energy Environ. Sci.* **2015**, *8*, 3374.
[38] K. Kerman, B. K. Lai, S. Ramanathan, *Adv. Energy Mater.* **2012**, *2*, 656.
[39] P. C. Su, C. C. Chao, J. H. Shim, R. Fasching, F. B. Prinz, *Nano Lett.* **2008**, *8*, 2289.
[40] J. G. Lee, J. H. Park, Y. G. Shul, *Nat. Commun.* **2014**, *5*, 4045.
[41] C. Duan, D. Hook, Y. Chen, J. Tong, R. O'Hayre, *Energy Environ. Sci.* **2017**, *10*, 176.
[42] Y. Chen, Y. Bu, B. Zhao, Y. Zhang, D. Ding, R. Hu, T. Wei, B. Rainwater, Y. Ding, F. Chen, C. Yang, J. Liu, M. Liu, *Nano Energy* **2016**, *26*, 90.
[43] B. C. H. Steele, *Solid State Ionics* **2000**, *129*, 95.
[44] K. L. Duncan, K.-T. Lee, E. D. Wachsman, *J. Power Sources* **2011**, *196*, 2445.
[45] D. H. Myung, J. Hong, K. Yoon, B. K. Kim, H. W. Lee, J. H. Lee, J. W. Son, *J. Power Sources* **2012**, *206*, 91.
[46] B. Dalslet, P. Blennow, P. V. Hendriksen, N. Bonanos, D. Lybye, M. Mogensen, *J. Solid State Electrochem.* **2006**, *10*, 547.
[47] K. Huang, M. Feng, J. B. Goodenough, C. Milliken, *J. Electrochem. Soc.* **1997**, *144*, 3620.
[48] S. Sanna, V. Esposito, J. W. Andreasen, J. Hjelm, W. Zhang, T. Kasama, S. B. Simonsen, M. Christensen, S. Linderoth, N. Pryds, *Nat. Mater.* **2015**, *14*, 500.
[49] J. Zhang, C. Lenser, N. H. Menzler, O. Guillon, *Solid State Ionics* **2020**, *344*, 115138.
[50] D. Lybye, F. W. Poulsen, M. Mogensen, *Solid State Ionics* **2000**, *128*, 91.
[51] D. W. Jung, K. L. Duncan, E. D. Wachsman, *Acta Mater.* **2010**, *58*, 355.
[52] T. Wei, P. Singh, Y. Gong, J. B. Goodenough, Y. Huang, K. Huang, *Energy Environ. Sci.* **2014**, *7*, 1680.

[53] L. Yang, S. Wang, K. Blinn, M. Liu, Z. Liu, Z. Cheng, M. Liu, *Science* **2009**, *326*, 126.
[54] R. Nédélec, S. Uhlenbruck, D. Sebold, V. A. C. Haanappel, H. P. Buchkremer, D. Stöver, *J. Power Sources* **2012**, *205*, 157.
[55] T. van Gestel, D. Sebold, H. P. Buchkremer, *J. Eur. Ceram. Soc.* **2015**, *35*, 1505.
[56] Z. Lu, J. Hardy, J. Templeton, J. Stevenson, D. Fisher, N. Wu, A. Ignatiev, *J. Power Sources* **2012**, *210*, 292.
[57] D. Yang, X. Zhang, S. Nikumb, C. Decès-Petit, R. Hui, R. Maric, D. Ghosh, *J. Power Sources* **2007**, *164*, 182.
[58] C. Lenser, H. Jeong, Y. J. Sohn, N. Russner, O. Guillon, N. H. Menzler, *J. Am. Ceram. Soc.* **2018**, *101*, 739.
[59] A. Tsoga, A. Gupta, A. Naoumidis, P. Nikolopoulos, *Acta Mater.* **2000**, *48*, 4709.
[60] A. Tsoga, A. Naoumidis, D. Stöver, *Solid State Ionics* **2000**, *135*, 403.
[61] H. Mitsuyasu, Y. Nonaka, K. Eguchi, *Solid State Ionics* **1998**, *113–115*, 279.
[62] R. Doshi, V. L. Richards, J. D. Carter, X. Wang, M. Krumpelt, *J. Electrochem. Soc.* **1999**, *146*, 1273.
[63] C. Xia, F. Chen, M. Liu, *Electrochem. Solid-State Lett.* **2001**, *4*, A52.
[64] C. Sun, R. Hui, J. Roller, *J. Solid State Electrochem.* **2010**, *14*, 1125.
[65] Y. Chen, W. Zhou, D. Ding, M. Liu, F. Ciucci, M. Tade, Z. Shao, *Adv. Energy Mater.* **2015**, *5*, 1500537.
[66] R. Jacobs, T. Mayeshiba, J. Booske, D. Morgan, *Adv. Energy Mater.* **2018**, *8*, 1702708.
[67] N. Mahato, A. Banerjee, A. Gupta, S. Omar, K. Balani, *Prog. Mater. Sci.* **2015**, *72*, 141.
[68] F. S. Baumann, J. Fleig, H. U. Habermeier, J. Maier, *Solid State Ionics* **2006**, *177*, 3187.
[69] S. B. Adler, *Chem. Rev.* **2004**, *104*, 4791.
[70] C. Xia, W. Rauch, F. Chen, M. Liu, *Solid State Ionics* **2002**, *149*, 11.
[71] Z. Shao, S. M. Haile, *Nature* **2004**, *431*, 170.
[72] L. Dieterle, P. Bockstaller, D. Gerthsen, J. Hayd, E. Ivers-Tiffée, U. Guntow, *Adv. Energy Mater.* **2011**, *1*, 249.
[73] C. Nicollet, A. Flura, V. Vibhu, A. Rougier, J. M. Bassat, J. C. Grenier, *Int. J. Hydrogen Energy* **2016**, *41*, 15538.
[74] A. Samson, M. Søgaard, R. Knibbe, N. Bonanos, *J. Electrochem. Soc.* **2011**, *158*, B650.
[75] D. Marinha, J. Hayd, L. Dessemond, E. Ivers-Tiffée, E. Djurado, *J. Power Sources* **2011**, *196*, 5084.
[76] A. J. Darbandi, H. Hahn, *Solid State Ionics* **2009**, *180*, 1379.
[77] R. Zeng, Y. Huang, *Int. J. Hydrogen Energy* **2017**, *42*, 7220.
[78] I. Jang, H. Lee, R. Tamarany, H. Yoon, C. Kim, S. Kim, C.-W. Lee, T. Song, U. Paik, *Chem. Mater.* **2020**, *32*, 3841.
[79] S. Choi, S. Yoo, J. Kim, S. Park, A. Jun, S. Sengodan, J. Kim, J. Shin, H. Y. Jeong, Y. Choi, G. Kim, M. Liu, *Sci. Rep.* **2013**, *3*, 2426.
[80] S. Yoo, A. Jun, Y.-W. W. Ju, D. Odkhuu, J. Hyodo, H. Y. Jeong, N. Park, J. Shin, T. Ishihara, G. Kim, *Angew. Chem., Int. Ed.* **2014**, *53*, 13064.
[81] G. Taillades, J. Dailly, M. Taillades-Jacquin, F. Mauvy, A. Essouhmi, M. Marrony, C. Lalanne, S. Fourcade, D. J. Jones, J.-C. Grenier, J. Rozière, *Fuel Cells* **2009**, *10*, 166.
[82] N. Hildenbrand, P. Nammensma, D. H. A. Blank, H. J. M. Bouwmeester, B. A. Boukamp, *J. Power Sources* **2013**, *238*, 442.
[83] D. Mesguich, J. M. Bassat, C. Aymonier, A. Brüll, L. Dessemond, E. Djurado, *Electrochim. Acta* **2013**, *87*, 330.
[84] C. Ferchaud, J. C. Grenier, Y. Zhang-Steenwinkel, M. M. A. Van Tuel, F. P. F. Van Berkel, J. M. Bassat, *J. Power Sources* **2011**, *196*, 1872.
[85] S. P. Jiang, *J. Mater. Sci.* **2008**, *43*, 6799.
[86] S. P. Jiang, J. P. Zhang, K. Foger, *J. Electrochem. Soc.* **2000**, *147*, 3195.
[87] I. Kojima, H. Adachi, I. Yasumori, *Surf. Sci.* **1983**, *130*, 50.
[88] A. N. Petrov, O. F. Kononchuk, A. v. Andreev, V. A. Cherepanov, P. Kofstad, *Solid State Ionics* **1995**, *80*, 189.
[89] M. Søgaard, P. V. Hendriksen, M. Mogensen, F. W. Poulsen, E. Skou, *Solid State Ionics* **2006**, *177*, 3285.
[90] L. W. Tai, M. M. Nasrallah, H. U. Anderson, D. M. Sparlin, S. R. Sehlin, *Solid State Ionics* **1995**, *76*, 273.
[91] Y. Zhang, B. Chen, D. Guan, M. Xu, R. Ran, M. Ni, W. Zhou, *Nature* **2021**, *591*, 246.
[92] M. Khoshkalam, Đ. Tripković, X. Tong, M. A. Faghihi-Sani, M. Chen, P. V. Hendriksen, *J. Power Sources* **2020**, *457*, 228035.
[93] D. Chen, S. R. Bishop, H. L. Tuller, *J. Electroceram.* **2012**, *28*, 62.
[94] S. R. Bishop, T. S. Stefanik, H. L. Tuller, *Phys. Chem. Chem. Phys.* **2011**, *13*, 10165.
[95] P. v Hendriksen, J. R. Høgsberg, A. M. Kjeldsen, B. F. Sørensen, H. G. Pedersen, *Advances in Solid Oxide Fuel Cells II: Ceramic Engineering and Science Proceedings* (Ed: N. P. Bansal), APA, Florida **2008**, p. 347.
[96] Z. Shao, W. Yang, Y. Cong, H. Dong, J. Tong, G. Xiong, *J. Membr. Sci.* **2000**, *172*, 177.
[97] J. Suntivich, K. J. May, H. A. Gasteiger, J. B. Goodenough, Y. Shao-Horn, *Science* **2011**, *334*, 1383.
[98] S. Svarcova, *Solid State Ionics* **2008**, *178*, 1787.
[99] C. Niedrig, S. Taufall, M. Burriel, W. Menesklou, S. F. Wagner, S. Baumann, E. Ivers-Tiffée, *Solid State Ionics* **2011**, *197*, 25.
[100] Z. Cai, Y. Kuru, J. W. Han, Y. Chen, B. Yildiz, *J. Am. Chem. Soc.* **2011**, *133*, 17696.
[101] A. A. Taskin, A. N. Lavrov, Y. Ando, *Appl. Phys. Lett.* **2005**, *86*, 091910.
[102] M. Burriel, J. Peña-Martínez, R. J. Chater, S. Fearn, A. V. Berenov, S. J. Skinner, J. A. Kilner, *Chem. Mater.* **2012**, *24*, 613.
[103] D. Parfitt, A. Chroneos, A. Tarancón, J. A. Kilner, *J. Mater. Chem.* **2011**, *21*, 2183.
[104] G. Kim, S. Wang, A. J. Jacobson, L. Reimus, P. Brodersen, C. A. Mims, *J. Mater. Chem.* **2007**, *17*, 2500.
[105] A. Tarancón, D. Marrero-López, J. Peña-Martínez, J. C. Ruiz-Morales, P. Núñez, *Solid State Ionics* **2008**, *179*, 611.
[106] J.-H. Kim, A. Manthiram, *J. Electrochem. Soc.* **2008**, *155*, B385.
[107] K. Zhang, L. Ge, R. Ran, Z. Shao, S. Liu, *Acta Mater.* **2008**, *56*, 4876.
[108] D. Chen, R. Ran, K. Zhang, J. Wang, Z. Shao, *J. Power Sources* **2009**, *188*, 96.
[109] L. Zhao, J. Shen, B. He, F. Chen, C. Xia, *Int. J. Hydrogen Energy* **2011**, *36*, 3658.
[110] L. Liu, R. Guo, C. Wang, C. Zhang, Y. Yang, S. Wang, *J. Solid State Electrochem.* **2014**, *18*, 2771.
[111] F. Jin, Y. Shen, R. Wang, T. He, *J. Power Sources* **2013**, *234*, 244.
[112] L. Jiang, T. Wei, R. Zeng, W. X. Zhang, Y. H. Huang, *J. Power Sources* **2013**, *232*, 279.
[113] J. M. Bassat, P. Odier, A. Villesuzanne, C. Marin, M. Pouchard, *Solid State Ionics* **2004**, *167*, 341.
[114] G. M. Rupp, A. K. Opitz, A. Nenning, A. Limbeck, J. Fleig, *Nat. Mater.* **2017**, *16*, 640.
[115] J. Hyodo, K. Tominaga, Y. W. Ju, S. Ida, T. Ishihara, *Solid State Ionics* **2014**, *256*, 5.
[116] L. Wang, R. Merkle, J. Maier, T. Acartürk, U. Starke, *Appl. Phys. Lett.* **2009**, *94*, 071908.
[117] M. Burriel, G. Garcia, J. Santiso, J. A. Kilner, R. J. Chater, S. J. Skinner, *J. Mater. Chem.* **2008**, *18*, 416.
[118] E. Boehm, J.-M. Bassat, P. Dordor, F. Mauvy, J.-C. Grenier, Ph. Stevens, *Solid State Ionics* **2005**, *176*, 2717.
[119] G. Amow, S. J. Skinner, *J. Solid State Electrochem.* **2006**, *10*, 538.
[120] A. Montenegro-Hernández, J. Vega-Castillo, L. Mogni, A. Caneiro, *Int. J. Hydrogen Energy* **2011**, *36*, 15704.
[121] B. Philippeau, F. Mauvy, C. Mazataud, S. Fourcade, J. C. Grenier, *Solid State Ionics* **2013**, *249–250*, 17.
[122] J. G. Railsback, Z. Gao, S. A. Barnett, *Solid State Ionics* **2015**, *274*, 134.

[123] M. Sase, K. Yashiro, K. Sato, J. Mizusaki, T. Kawada, N. Sakai, K. Yamaji, T. Horita, H. Yokokawa, *Solid State Ionics* **2008**, *178*, 1843.
[124] S. Stämmler, R. Merkle, J. Maier, *J. Electrochem. Soc.* **2017**, *164*, F454.
[125] E. J. Crumlin, E. Mutoro, S. J. Ahn, G. J. La O, D. N. Leonard, A. Borisevich, M. D. Biegalski, H. M. Christen, Y. Shao-Horn, *J. Phys. Chem. Lett.* **2010**, *1*, 3149.
[126] W. Ma, J. J. Kim, N. Tsvetkov, T. Daio, Y. Kuru, Z. Cai, Y. Chen, K. Sasaki, H. L. Tuller, B. Yildiz, *J. Mater. Chem. A* **2015**, *3*, 207.
[127] Y. Chen, Z. Cai, Y. Kuru, W. Ma, H. L. Tuller, B. Yildiz, *Adv. Energy Mater.* **2013**, *3*, 1221.
[128] D. Lee, Y. L. Lee, W. T. Hong, M. D. Biegalski, D. Morgan, Y. Shao-Horn, *J. Mater. Chem. A* **2015**, *3*, 2144.
[129] J. T. S. Irvine, D. Neagu, M. C. Verbraeken, C. Chatzichristodoulou, C. Graves, M. B. Mogensen, *Nat. Energy* **2016**, *1*, 15014.
[130] W. Z. Zhu, S. C. Deevi, *Mater. Sci. Eng., A* **2003**, *362*, 228.
[131] S. P. Jiang, S. H. Chan, *J. Mater. Sci.* **2004**, *39*, 4405.
[132] H. Zhu, R. J. Kee, V. M. Janardhanan, O. Deutschmann, D. G. Goodwin, *J. Electrochem. Soc.* **2005**, *152*, A2427.
[133] T. Hibino, A. Hashimoto, T. Inoue, J. I. Tokuno, S. I. Yoshida, M. Sano, *Science* **2000**, *288*, 2031.
[134] E. P. Murray, T. Tsai, S. A. Barnett, *Nature* **1999**, *400*, 649.
[135] A. Utz, A. Leonide, A. Weber, E. Ivers-Tiffée, *J. Power Sources* **2011**, *196*, 7217.
[136] M. R. Somalu, V. Yufit, D. Cumming, E. Lorente, N. P. Brandon, *Int. J. Hydrogen Energy* **2011**, *36*, 5557.
[137] K. Yamamoto, T. Hashishin, M. Matsuda, N. Qiu, Z. Tan, S. Ohara, *Nano Energy* **2014**, *6*, 103.
[138] C. Duan, R. J. Kee, H. Zhu, C. Karakaya, Y. Chen, S. Ricote, A. Jarry, E. J. Crumlin, D. Hook, R. Braun, N. P. Sullivan, R. O'Hayre, *Nature* **2018**, *557*, 217.
[139] C. Duan, J. Huang, N. Sullivan, R. O'Hayre, *Appl. Phys. Rev.* **2020**, *7*, 011314.
[140] E. Fabbri, D. Pergolesi, E. Traversa, *Chem. Soc. Rev.* **2010**, *39*, 4355.
[141] K. D. Kreuer, *Annu. Rev. Mater. Res.* **2003**, *33*, 333.
[142] L. Malavasi, C. A. J. Fisher, M. S. Islam, *Chem. Soc. Rev.* **2010**, *39*, 4370.
[143] Y. Meng, J. Gao, Z. Zhao, J. Amoroso, J. Tong, K. S. Brinkman, *J. Mater. Sci.* **2019**, *54*, 9291.
[144] H. Iwahara, T. Esaka, H. Uchida, N. Maeda, *Solid State Ionics* **1981**, *3–4*, 359.
[145] H. Iwahara, H. Uchida, K. Ono, K. Ogaki, *J. Electrochem. Soc.* **1988**, *135*, 529.
[146] M. J. Scholten, J. Schoonman, J. C. van Miltenburg, H. A. J. Oonk, *Solid State Ionics* **1993**, *61*, 83.
[147] N. Zakowsky, S. Williamson, J. T. S. Irvine, *Solid State Ionics* **2005**, *176*, 3019.
[148] D. Medvedev, A. Murashkina, E. Pikalova, A. Demin, A. Podias, P. Tsiakaras, *Prog. Mater. Sci.* **2014**, *60*, 72.
[149] K. H. Ryu, S. M. Haile, *Solid State Ionics* **1999**, *125*, 355.
[150] S. Tao, J. T. S. Irvine, *Adv. Mater.* **2006**, *18*, 1581.
[151] P. Babilo, S. M. Haile, *J. Am. Ceram. Soc.* **2005**, *88*, 2362.
[152] M. Biswas, H. An, S. M. Choi, J. W. Son, J. H. Lee, B. K. Kim, H. W. Lee, K. J. Yoon, *Ceram. Int.* **2016**, *42*, 10476.
[153] Z. Sun, E. Fabbri, L. Bi, E. Traversa, *J. Am. Ceram. Soc.* **2012**, *95*, 627.
[154] K. Katahira, Y. Kohchi, T. Shimura, H. Iwahara, *Solid State Ionics* **2000**, *138*, 91.
[155] J. Kim, S. Sengodan, G. Kwon, D. Ding, J. Shin, M. Liu, G. Kim, *ChemSusChem* **2014**, *7*, 2811.
[156] N. T. Q. Nguyen, H. H. Yoon, *J. Power Sources* **2013**, *231*, 213.
[157] X. Lv, H. Chen, W. Zhou, S. D. Li, Z. Shao, *J. Mater. Chem. A* **2020**, *8*, 11292.
[158] A. VahidMohammadi, Z. Cheng, *J. Electrochem. Soc.* **2015**, *162*, F803.
[159] M. A. Azimova, S. McIntosh, *Solid State Ionics* **2009**, *180*, 160.
[160] J. Tong, D. Clark, L. Bernau, A. Subramaniyan, R. O'Hayre, *Solid State Ionics* **2010**, *181*, 1486.
[161] S. Ricote, N. Bonanos, A. Manerbino, W. G. Coors, *Int. J. Hydrogen Energy* **2012**, *37*, 7954.
[162] S. Nikodemski, J. Tong, R. O'Hayre, *Solid State Ionics* **2013**, *253*, 201.
[163] R. Murphy, Y. Zhou, L. Zhang, L. Soule, W. Zhang, Y. Chen, M. Liu, *Adv. Funct. Mater.* **2020**, *30*, 2002265.
[164] J. Dailly, S. Fourcade, A. Largeteau, F. Mauvy, J. C. Grenier, M. Marrony, *Electrochim. Acta* **2010**, *55*, 5847.
[165] L. Zhao, B. He, Y. ling, Z. Xun, R. Peng, G. Meng, X. Liu, *Int. J. Hydrogen Energy* **2010**, *35*, 3769.
[166] G. Goupil, T. Delahaye, G. Gauthier, B. Sala, F. L. Joud, *Solid State Ionics* **2012**, *209–210*, 36.
[167] M. Shang, J. Tong, R. O'Hayre, *RSC Adv.* **2013**, *3*, 15769.
[168] H. G. Seo, Y. Choi, W. C. Jung, *Adv. Energy Mater.* **2018**, *8*, 1703647.
[169] T. Wu, Y. Zhao, R. Peng, C. Xia, *Electrochim. Acta* **2009**, *54*, 4888.
[170] S. Upasen, P. Batocchi, F. Mauvy, A. Slodczyk, P. Colomban, *Ceram. Int.* **2015**, *41*, 14137.
[171] M. Papac, V. Stevanović, A. Zakutayev, R. O'Hayre, *Nat. Mater.* **2021**, *20*, 301.
[172] R. Zohourian, R. Merkle, G. Raimondi, J. Maier, *Adv. Funct. Mater.* **2018**, *28*, 1801241.
[173] A. Løken, S. Ricote, S. Wachowski, *Crystals* **2018**, *8*, 365.
[174] A. v. Kasyanova, L. R. Tarutina, A. O. Rudenko, J. G. Lyagaeva, D. A. Medvedev, *Russ. Chem. Rev.* **2020**, *89*, 667.
[175] G. C. Mather, D. Muñoz-Gil, J. Zamudio-García, J. M. Porras-Vázquez, D. Marrero-López, D. Pérez-Coll, *Appl. Sci.* **2021**, *11*, 5363.
[176] E. Fabbri, L. Bi, D. Pergolesi, E. Traversa, *Adv. Mater.* **2012**, *24*, 195.
[177] B. Lin, H. Ding, Y. Dong, S. Wang, X. Zhang, D. Fang, G. Meng, *J. Power Sources* **2009**, *186*, 58.
[178] W. Sun, Z. Zhu, Y. Jiang, Z. Shi, L. Yan, W. Liu, *Int. J. Hydrogen Energy* **2011**, *36*, 9956.
[179] W. Sun, L. Yan, B. Lin, S. Zhang, W. Liu, *J. Power Sources* **2010**, *195*, 3155.
[180] L. Yang, S. Wang, X. Lou, M. Liu, *Int. J. Hydrogen Energy* **2011**, *36*, 2266.
[181] N. Bausá, C. Solís, R. Strandbakke, J. M. Serra, *Solid State Ionics* **2017**, *306*, 62.
[182] G. Li, H. Jin, Y. Cui, L. Gui, B. He, L. Zhao, *J. Power Sources* **2017**, *341*, 192.
[183] S. Ricote, N. Bonanos, F. Lenrick, R. Wallenberg, *J. Power Sources* **2012**, *218*, 313.
[184] S. Ricote, N. Bonanos, P. M. Rørvik, C. Haavik, *J. Power Sources* **2012**, *209*, 172.
[185] L. Rioja-Monllor, S. Ricote, C. Bernuy-Lopez, T. Grande, R. O'Hayre, M. A. Einarsrud, *Inorganics* **2018**, *6*, 83.
[186] M. Liang, Y. Zhu, Y. Song, D. Guan, Z. Luo, G. Yang, S. P. Jiang, W. Zhou, R. Ran, Z. Shao, *Adv. Mater.* **2021**, 2106379.
[187] Y. Song, J. Liu, Y. Wang, D. Guan, A. Seong, M. Liang, M. J. Robson, X. Xiong, Z. Zhang, G. Kim, Z. Shao, F. Ciucci, *Adv. Energy Mater.* **2021**, *11*, 2101899.
[188] H. Shi, C. Su, X. Xu, Y. Pan, G. Yang, R. Ran, Z. Shao, *Small* **2021**, *17*, 2101872.
[189] R. Strandbakke, V. A. Cherepanov, A. Y. Zuev, D. S. Tsvetkov, C. Argirusis, G. Sourkouni, S. Prünte, T. Norby, *Solid State Ionics* **2015**, *278*, 120.
[190] H. Téllez Lozano, J. Druce, S. J. Cooper, J. A. Kilner, *Sci. Technol. Adv. Mater.* **2017**, *18*, 977.
[191] E. Vøllestad, M. Schrade, J. Segalini, R. Strandbakke, T. Norby, *J. Mater. Chem. A* **2017**, *5*, 15743.
[192] R. Merkle, D. Poetzsch, J. Maier, *ECS Trans.* **2015**, *66*, 95.
[193] L. Bi, S. P. Shafi, E. H. Da'as, E. Traversa, *Small* **2018**, *14*, 1801231.
[194] N. Wang, S. Hinokuma, T. Ina, C. Zhu, H. Habazaki, Y. Aoki, *J. Mater. Chem. A* **2020**, *8*, 11043.

[195] Y. Chen, S. Yoo, K. Pei, D. Chen, L. Zhang, B. deGlee, R. Murphy, B. Zhao, Y. Zhang, Y. Chen, M. Liu, *Adv. Funct. Mater.* **2018**, *28*, 1704907.
[196] S. D. Kim, S. H. Hyun, J. Moon, J. H. Kim, R. H. Song, *J. Power Sources* **2005**, *139*, 67.
[197] T. Onishi, D. Han, Y. Noda, N. Hatada, M. Majima, T. Uda, *Solid State Ionics* **2018**, *317*, 127.
[198] C. T. Shen, Y. H. Lee, K. Xie, C. P. Yen, J. W. Jhuang, K. R. Lee, S. W. Lee, C. J. Tseng, *Ceram. Int.* **2017**, *43*, S671.
[199] K. Ueno, N. Hatada, D. Han, T. Uda, *J. Mater. Chem. A* **2019**, *7*, 7232.
[200] D. Han, L. Jiang, P. Zhong, *Int. J. Hydrogen Energy* **2021**, *46*, 8767.
[201] A. Bieberle-Hütter, D. Beckel, A. Infortuna, U. P. Muecke, J. L. M. Rupp, L. J. Gauckler, S. Rey-Mermet, P. Muralt, N. R. Bieri, N. Hotz, M. J. Stutz, D. Poulikakos, P. Heeb, P. Müller, A. Bernard, R. Gmür, T. Hocker, *J. Power Sources* **2008**, *177*, 123.
[202] A. Evans, A. Bieberle-Hütter, H. Galinski, J. L. M. Rupp, T. Ryll, B. Scherrer, R. Tölke, L. J. Gauckler, *Monatsh. Chem.* **2009**, *140*, 975.
[203] F. Chiabrera, I. Garbayo, N. Alayo, A. Tarancón, SPIE Microtechnologies (Eds: L. Fonseca, M. Prunnila, E. Peiner), Barcelona, Spain **2017**, p. 102460S.
[204] Z. Shao, S. M. Haile, J. Ahn, P. D. Ronney, Z. Zhan, S. A. Barnett, *Nature* **2005**, *435*, 795.
[205] H. Huang, M. Nakamura, P. Su, R. Fasching, Y. Saito, F. B. Prinz, *J. Electrochem. Soc.* **2007**, *154*, B20.
[206] Y. Li, P. C. Su, L. M. Wong, S. Wang, *J. Power Sources* **2014**, *268*, 804.
[207] M. Tsuchiya, B. K. Lai, S. Ramanathan, *Nat. Nanotechnol.* **2011**, *6*, 282.
[208] C. C. Chao, C. M. Hsu, Y. Cui, F. B. Prinz, *ACS Nano* **2011**, *5*, 5692.
[209] K. Kerman, B. K. Lai, S. Ramanathan, *J. Power Sources* **2011**, *196*, 6214.
[210] A. C. Johnson, B. K. Lai, H. Xiong, S. Ramanathan, *J. Power Sources* **2009**, *186*, 252.
[211] A. Evans, C. Benel, A. J. Darbandi, H. Hahn, J. Martynczuk, L. J. Gauckler, M. Prestat, *Fuel Cells* **2013**, *13*, 441.
[212] J. H. Joo, G. M. Choi, *J. Power Sources* **2008**, *182*, 589.
[213] X. Wang, H. Huang, T. Holme, X. Tian, F. B. Prinz, *J. Power Sources* **2008**, *175*, 75.
[214] S. Kang, P. C. Su, Y. I. Park, Y. Saito, F. B. Prinz, *J. Electrochem. Soc.* **2006**, *153*, A554.
[215] B. K. Lai, K. Kerman, S. Ramanathan, *J. Power Sources* **2011**, *196*, 6299.
[216] I. Chang, S. Ji, J. Park, M. H. Lee, S. W. Cha, *Adv. Energy Mater.* **2015**, *5*, 1402251.
[217] K. Bae, D. Y. Jang, H. J. Jung, J. W. Kim, J. W. Son, J. H. Shim, *J. Power Sources* **2014**, *248*, 1163.
[218] U. P. Muecke, D. Beckel, A. Bernard, A. Bieberle-Hütter, S. Graf, A. Infortuna, P. Müller, J. L. M. Rupp, J. Schneider, L. J. Gauckler, *Adv. Funct. Mater.* **2008**, *18*, 3158.
[219] J. H. Shim, C. C. Chao, H. Huango, F. B. Prinz, *Chem. Mater.* **2007**, *19*, 3850.
[220] J. M. Vohs, R. J. Gorte, *Adv. Mater.* **2009**, *21*, 943.
[221] T. Tsai, S. A. Barnett, *J. Electrochem. Soc.* **1995**, *142*, 3084.
[222] C. W. Kwon, J. W. Son, J. H. Lee, H. M. Kim, H. W. Lee, K. B. Kim, *Adv. Funct. Mater.* **2011**, *21*, 1154.
[223] V. T. Srikar, K. T. Turner, T. Y. A. Ie, S. M. Spearing, *J. Power Sources* **2004**, *125*, 62.
[224] C. D. Baertsch, K. F. Jensen, J. L. Hertz, H. L. Tuller, S. T. Vengallatore, S. M. Spearing, M. A. Schmidt, *J. Mater. Res.* **2004**, *19*, 2604.
[225] J. D. Baek, K. Y. Liu, P. C. Su, *J. Mater. Chem. A* **2017**, *5*, 18414.
[226] M. V. F. Schlupp, A. Evans, J. Martynczuk, M. Prestat, *Adv. Energy Mater.* **2014**, *4*, 1301383.
[227] H. Galinski, T. Ryll, P. Elser, J. L. M. Rupp, A. Bieberle-Hütter, L. J. Gauckler, *Phys. Rev. B* **2010**, *82*, 235415.
[228] B. K. Lai, K. Kerman, S. Ramanathan, *J. Power Sources* **2011**, *196*, 1826.
[229] S. H. Choi, S. W. Kim, C. S. Hwang, M. H. Lee, *Fuel Cells* **2014**, *14*, 332.
[230] J. Hayd, E. Ivers-Tiffée, *J. Electrochem. Soc.* **2013**, *160*, F1197.
[231] J. Hayd, H. Yokokawa, E. Ivers-Tiffée, *J. Electrochem. Soc.* **2013**, *160*, F351.
[232] A. Cavallaro, S. S. Pramana, E. Ruiz-Trejo, P. C. Sherrell, E. Ware, J. A. Kilner, S. J. Skinner, *Sustainable Energy Fuels* **2018**, *2*, 862.
[233] X. Chen, N. J. Wu, D. L. Ritums, A. Ignatiev, *Thin Solid Films* **1999**, *342*, 61.
[234] J. Januschewsky, M. Ahrens, A. Opitz, F. Kubel, J. Fleig, *Adv. Funct. Mater.* **2009**, *19*, 3151.
[235] Y. Takagi, S. Adam, S. Ramanathan, *J. Power Sources* **2012**, *217*, 543.
[236] Y. Takagi, B. K. Lai, K. Kerman, S. Ramanathan, *Energy Environ. Sci.* **2011**, *4*, 3473.
[237] Z. Wang, Y. Gu, L. Zheng, J. Hou, H. Zheng, S. Sun, L. Wang, *Adv. Mater.* **2021**, 2106776.
[238] J. Liu, W. Luo, L. Wang, J. Zhang, X. Fu, J. Luo, *Adv. Funct. Mater.* **2022**, 2110748.
[239] Y.-L. Lee, J. Kleis, J. Rossmeisl, Y. Shao-Horn, D. Morgan, *Energy Environ. Sci.* **2011**, *4*, 3966.
[240] C. Nicollet, C. Toparli, G. F. Harrington, T. Defferriere, B. Yildiz, H. L. Tuller, *Nat. Catal.* **2020**, *3*, 913.
[241] C. Lenser, Q. Lu, E. Crumlin, H. Bluhm, B. Yildiz, *J. Phys. Chem. C* **2018**, *122*, 4841.

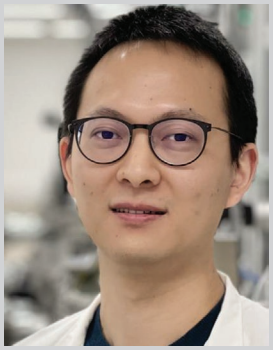

Jun Zhang is currently a postdoctoral researcher at the Department of Energy Conversion and Storage (DTU Energy) of Technical University of Denmark. He received his Ph.D. from RWTH Aachen University and Forschungszentrum Jülich in Germany in 2020, for the research of using ceramic processing techniques to develop thin film electrolyte (gadolinium-doped ceria) for solid oxide fuel cells. After that, he joined DTU Energy to focus on the understanding of surface oxygen reduction reaction mechanism of electrode materials for protonic ceramic fuel cells.

Sandrine Ricote is an associate research professor at Colorado School of Mines (CSM). She earned her Ph.D. from the University of Burgundy (France) for her research on the characterization of high-temperature proton-conducting ceramic materials ($BaCe_{0.9-x}Zr_xY_{0.1}O_{2.95}$). She completed a four-year appointment at the Technical University of Denmark where she developed proton-conducting membranes and electrode materials. She joined CSM in 2012 and has been working since on the development of protonic ceramic fuel/electrolysis cells and membrane reactors, and other high-temperature ion conductors. She was the Chair of the Colorado Section of the American Ceramic Society and is now a board member.

Peter Vang Hendriksen is educated at the Technical University of Denmark from where he obtained his Ph.D. degree in 1993 in the area of magnetic properties of nanoparticles. He then moved to Risø National Laboratory to work on development of solid oxide fuel cells and has since then been active in this field. He is currently heading the section for Solid State Chemistry at Department of Energy Conversion and Storage at DTU, where the research is centered on solid oxide cells, involving both oxide ion and proton conducting materials considering electrolysis as well as fuel cell operation.

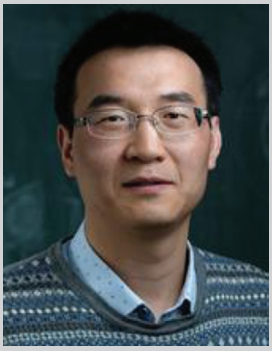

Yunzhong Chen is a professor at Institute of Physics, Chinese Academy of Sciences. His research focuses on the creation and understanding of interface phenomena in atomically engineered oxide heterostructures for high electronic and ionic conductivity, ferromagnetism, and enhanced catalytic activity.